ELSEVIER

J. Non-Newtonian Fluid Mech. 139 (2006) 1–20

Journal of Non-Newtonian Fluid Mechanics

www.elsevier.com/locate/jnnfm

Numerical investigation of the velocity overshoots in the flow of viscoelastic fluids inside a smooth contraction

A. Afonso [a], F.T. Pinho [a,b,*]

[a] *Centro de Estudos de Fenómenos de Transporte, Faculdade de Engenharia da Universidade do Porto, Rua Dr. Roberto Frias s/n, 4200-465 Porto, Portugal*
[b] *Universidade do Minho, Largo do Paço, 4704-553 Braga, Portugal*

Received 9 December 2005; received in revised form 26 May 2006; accepted 29 May 2006

Abstract

Large velocity overshoots with very strong velocity gradients appear near the side walls of a smooth contraction (contraction ratio 2.86:1) following a square duct and preceding a plane sudden expansion of large expansion ratio ($D/d = 1.43$), when viscoelastic fluids flow in the laminar regime, as observed experimentally by Poole et al. [R.J. Poole, M.P. Escudier, A. Afonso, F.T. Pinho, Laminar viscoelastic flow over a backward-facing step, in: Proceedings of the XIV International Congress on Rheology, Paper NF-06, Seoul, South Korea, 2004; R.J. Poole, M.P. Escudier, P.J. Oliveira, Laminar flow of a viscoelastic shear-thinning liquid through a plane sudden expansion preceded by a gradual contraction, Proc. R. Soc. London Series A 461 (2005) 3827–3845; R.J. Poole, M.P. Escudier, A. Afonso, F.T. Pinho, Laminar flow of a viscoelastic shear-thinning liquid over a backward-facing step preceded by a gradual contraction, Phys. Fluids, submitted for publication]. To help understand this phenomenon an extensive numerical investigation was undertaken in the five parameter space of a fluid described by the Phan-Thien–Tanner (PTT) constitutive equation with non-zero second normal-stress difference ($N_2 \neq 0$ due to $\xi \neq 0$) and a solvent contribution.

The numerical simulations were able to qualitatively capture the velocity overshoots on the *XZ*-centreline profiles, and observed also overshoots on the *XY*-mid-plane and the so far unreported enhanced velocity peak at the duct corners. For this particular geometry the overshoots took place for particular combinations of the independent parameters, in particular they required large Weissenberg numbers, large second normal-stress differences, strain-hardening of the extensional viscosity and intense shear-thinning, together with non-negligible inertia. The parametric investigation also reports the variations of the three-dimensional velocity profiles which progressed from being rather flat shaped at low elasticity and high Reynolds numbers (typical of purely viscous behaviour) towards a slim almost triangular shape at high elasticity numbers.

Keywords: Viscoelasticity; Velocity overshoots; PTT model; Second normal-stress difference; Smooth contraction; Enstrophy

1. Introduction

The prediction of viscoelastic flows in complex geometries, such as in expansions or contractions, has both scientific interest and industrial relevance. The development of numerical methods to predict expansion flows for non-Newtonian fluids has been investigated by a number of different researchers. Halmos et al. [4,5] presented limited numerical results for axisymmetric sudden expansions and compared them with experiments, modeling the fluids as inelastic by the power-law equation. Power law fluids and axisymmetric sudden expansions were also considered by Pinho et al. [6] in their numerical investigation on the effects of expansion ratio, inlet Reynolds number and power law index upon pressure loss coefficients. In their experiments of 1976, Halmos and Boger [7] concluded that as viscoelastic fluids flow through a sudden expansion, they release some of their stored energy, expanding the main jet and compressing the recirculation region, leading to a shorter and weaker eddy.

Townsend and Walters [8] visualized the flowfield downstream of two-dimensional and three-dimensional sudden expansions for a 0.15 wt.% aqueous solution of polyacrylamide. Their numerical predictions with a Phan-Thien–Tanner model (PTT) were qualitatively in good agreement with the observed flow visualizations, but the work lacked detailed rheological and velocity data. Their conclusions regarding the role of viscoelasticity agreed with those of Halmos and Boger [7] in that elasticity of the polymer solutions damped the vortex activity and pushed the recirculation region against the corners of the expansion. The numerical simulations of Baloch et al. [9]

* Corresponding author.
E-mail addresses: aafonso@fe.up.pt (A. Afonso), fpinho@fe.up.pt (F.T. Pinho).

0377-0257/$ – see front matter © 2006 Elsevier B.V. All rights reserved.
doi:10.1016/j.jnnfm.2006.05.012

Nomenclature

a_F	neighbour cell coefficients of algebraic equations accounting for convection and diffusion
a_P	central cell coefficient of the algebraic equations
A	aspect ratio w/h
d	duct height at inlet (m)
D	downstream duct height (m)
El	elasticity number ($El \equiv We/Re_c = \lambda\eta_c/\rho H^2$)
$f(\tau_{kk})$	linear stress function in the Phan-Thien–Tanner model
h	step height (m)
N_1	first normal-stress difference (Pa)
N_2	second normal-stress difference (Pa)
p	pressure (Pa)
R	expansion ratio D/d
Re	zero shear rate Reynolds number ($\equiv\rho hU/\eta_0$)
Re_c	characteristic shear rate viscosity Reynolds number ($\equiv\rho hU/\eta_c$)
S	source terms of the algebraic equations
S_{ij}	rate of deformation tensor
t	time (s)
u	streamwise velocity (m s^{-1})
U	bulk velocity at expansion inlet (m s^{-1})
$\vec{U}$	velocity vector
V_P	volume of cell P
w	channel width (also duct height upstream of gradual contraction) (m)
We	Weissenberg number ($\equiv\lambda/T_{CH}$)
x	streamwise coordinate (m)
x_i	components of the orthogonal Cartesian coordinate system
XZ, XY	centreplanes
y	cross-stream coordinate (m)
Δy, Δz	mesh cell spacing in the y- and z-directions, respectively
z	spanwise coordinate (m)

Greek letters

β	ratio between the Newtonian solvent viscosity and total zero shear-rate viscosity
β_{li}	metric coefficients
$\dot{\gamma}_c$	characteristic shear rate ($\dot{\gamma}_c = U/h$)
δt	time step (s)
ε	extensibility parameter of Phan-Thien–Tanner model
ζ_l	components of the general non-orthogonal coordinate system
η_0	total zero-shear rate viscosity (Pa s)
η_P	polymer viscosity coefficient (Pa s)
η_S	Newtonian solvent viscosity (Pa s)
λ	relaxation time of fluid (s)
ξ	slip parameter of Phan-Thien–Tanner model
ρ	fluid density (kg m^{-3})
τ_{ij}	stress tensor (Pa)
$\vec{\omega}$	vorticity vector ($\vec{\omega} = \text{curl}\,\vec{U}$)
ω^2	enstrophy ($\omega^2 = \vec{\omega}\cdot\vec{\omega}$)

in two and three-dimensional expansions with PTT fluids also compared well with the experimental data of Townsend and Walters [8], and confirmed the role of viscoelasticity in suppressing vortex activity. They linked this suppression to the extrudate swell phenomenon and the first normal-stress difference coefficient.

Recently, Poole et al. [2] presented experimental observations for the flow of a 0.05% by weight polyacrylamide solution through a plane sudden expansion of expansion ratio (R = duct height downstream of expansion/duct height upstream of expansion = D/d, see Fig. 1) 4 and aspect ratio (A = width of duct/step height = w/h) 5.33. The plane sudden expansion was preceded immediately by a short gradual contraction from a long (120 hydraulic diameters in length) square duct. In contrast to the laminar flow of a Newtonian fluid, where the flowfield downstream of the expansion develops stable top-to-bottom asymmetry above a critical Reynolds number for an expansion ratio greater than 1.5, in the laminar flow of a viscoelastic fluid downstream of the expansion, the top-to-bottom asymmetry was greatly reduced, with very similar reattachment lengths for the two recirculation regions. The strong asymmetry for Newtonian fluids has been observed many times both experimentally [10–12] and numerically [13,14]. More significantly to this work, the viscoelastic flow unexpectedly developed a strongly three-dimensional jet-like structure, with side-to-side symmetry centred on the "vertical" symmetry plane of the contraction/expansion geometry (we will also refer to this as along the spanwise direction). Poole et al. [2] also reports that the nature of the flowfield within the contraction itself is found to be fundamentally different from that of Newtonian fluids, presenting remarkable new features: large velocity overshoots with very strong gradients appear near to the sidewalls that, due to their appearance, they have dubbed "cat's ears" (see Fig. 2). As the approach flow in the square duct was fully developed, it was speculated that the cat's ears were a consequence of the large normal-stress differences arising in highly viscoelastic liquids. Even though the magnitude of the secondary flows do not exceed at most 5% of the magnitude of the streamwise flow [15], secondary flows have been shown to be the dominant mechanism behind some unexpected phenomena, such as the experimen-

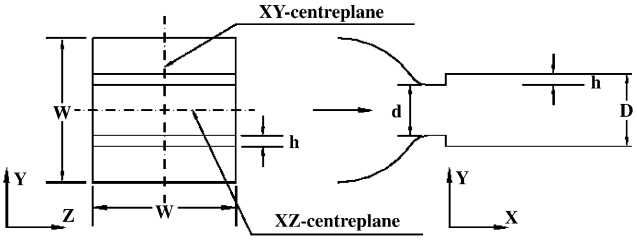

Fig. 1. Double backward-facing step geometry (from Poole et al. [1]).

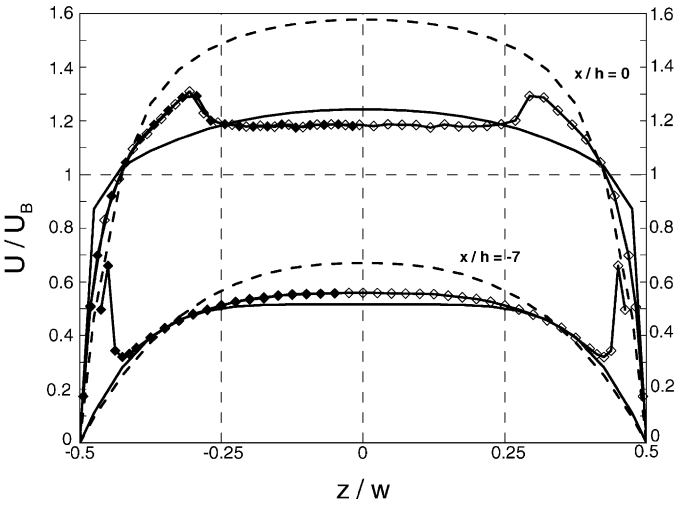

Fig. 2. Velocity profiles for $y/D=0$ (XZ-centreplane) within contraction ($x/h=-7.0$; $x/h=0$). Simulations for Newtonian fluid (solid line) and generalised Newtonian fluid (dashed line). 0.1% PAA, $Re=118$. Symbols represent the experimental data obtained by Poole et al. [1,3].

tally observed heat transfer enhancement with viscoelastic fluids in steady laminar flow [16,17] or enhanced mixing of polymer melts in ducts [18]. There is also experimental evidence that secondary flows practically do not require an increase in the energy input to drive the flow. Summary of patterns and review of these secondary flows for different tube geometries can be found in books by Tanner [19] and Leonov and Prokunin [20].

Guided by experience with Newtonian fluid flow [14], Poole et al. [3] presented an experimental and numerical investigation, in which the only difference to the previous work [2] was that the expansion geometry had a lower expansion ratio of 1.43, with the intention of avoiding the possibility of top-to-bottom asymmetry and so that one half of the geometry could be regarded as a backward-facing step. In that work [3], experimental observations for the flows of various polyacrylamide aqueous solutions (0.05, 0.1 and 0.4 wt.%) are compared with results from numerical simulations with inelastic and viscoelastic fluids (see Fig. 2). The purely viscous fluids were modeled as Newtonian and generalized Newtonian, with the viscosity function of the latter given by the Carreau–Yasuda model fit to the experimental rheology data. To represent the viscoelastic fluids, the PTT model of Phan-Thien–Tanner [21,22] with linear stress coefficient and zero second normal-stress difference coefficient was adopted, in an attempt to identify the physical mechanisms responsible for the appearance of large velocity overshoots.

Since the fluid dynamic predictions with all those fluids failed to show key features observed experimentally, those initial calculations were followed by an extensive parametric investigation of the effects of Weissenberg number, Reynolds number, shear-thinning and the extensibility (ε) and slip (ξ) parameters, in what constitutes the main objective of the present work. It is important to emphasize that this flow has been recently suggested as a benchmark for numerical calculations of three-dimensional confined viscoelastic fluid flows [23]. The rheology of the polymer solutions are here represented as the sum of a Newtonian solvent contribution with a full PTT polymer contribution.

The paper is organized as follows: in Sections 2–4 we briefly describe the general flow problem, present the governing equations and outline the numerical method used to simulate the flow of the viscoelastic fluids, respectively. In Section 5, the main results of the parametric investigation are presented and discussed to assess separately the effects of Weissenberg number, Reynolds number, the ratio of solvent to total viscosities, and parameters ε and ξ of the PTT model on the appearance of velocity overshoots near the walls. A summary of the main findings closes the paper in Section 6.

2. Flow geometry and computational mesh

The flow geometry, sketched in Fig. 1, is the same used in the experiments of Poole et al. [1,3] which is a modified version of that used by Escudier and Smith [24]. It consists of a plane sudden expansion preceded by a smooth contraction, having a mild contraction ratio of 2.86:1, and a long duct of square cross-section. The whole geometry has a constant width w of 80 mm, the contraction is 60 mm long and is made from two circular parts (50 mm radius followed by 11 mm radius). The inlet square duct is 80 mm × 80 mm and the inlet to the expansion is 28 mm × 80 mm ($d \times w$). The step height h is 6 mm and so the outlet rectangular duct is 40 mm × 80 mm ($D \times w$). This produces an expansion ratio ($R=D/d$) of 1.43 and an aspect ratio (w/h) of 13.33 so that the expansion acts essentially as a double backward-facing step, i.e. according to the literature for Newtonian fluids, the flow remains symmetric. Nevertheless, in order to capture any asymmetries the flow of viscoelastic fluids may have, all calculations reported here used a wall-to-wall computational domain in the cross-stream (y) and spanwise (z) directions (see Fig. 3).

The computational domain was chosen to map part of the square inlet duct down to the downstream channel, including the contraction and sudden expansion. The square duct was nearly 5 m long (62 inlet duct hydraulic diameters) and the downstream channel was 120 h in length, in both cases to ensure fully developed flows upstream and downstream of the contraction and backward-facing steps, respectively.

The calculations were carried out in three different meshes (Ml–M3). Mesh Ml was the mesh used in the viscoelastic calculations by Poole et al. [3]: the domain was mapped from wall to wall, in both the cross-stream and spanwise directions, with 40 blocks having a total of 102,000 cells corresponding to 1,020,000 degrees of freedom. There were 20 and 30 cells from wall to wall in the y- and z-directions, respectively, and the minimum cells sizes were $(\Delta y_{\min})/h=0.142$ and $(\Delta z_{\min})/h=0.397$, respectively. To give an idea of this mesh, Fig. 3 shows the mapping of the smooth contraction and sudden expansion in 2D and 3D views. M2 was a finer mesh in the y-direction, with 30 cells from wall to wall and minimum cell size of $(\Delta y_{\min})/h=0.083$, having a total of 191,700 cells corresponding to 1,917,000 degrees of freedom. Finally, mesh M3 had 10 blocks that mapped only a quarter of the geometry, i.e. from the two centre-planes of symmetry in the cross-stream and spanwise directions to the wall, with 20 cells in each direction. The corresponding minimum cells sizes were $(\Delta y_{\min})/h=0.083$ and $(\Delta z_{\min})/h=0.333$,

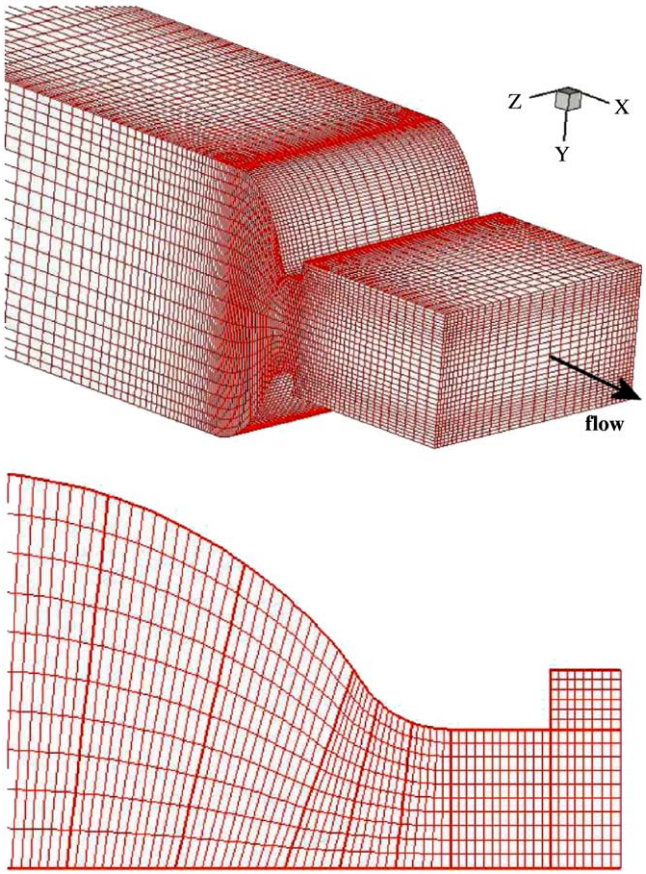

Fig. 3. Mesh M1 used for viscoelastic numerical simulations: view of contraction and expansion region and a detail of mesh in *XY* symmetry plane.

respectively. Mesh M3 had a total of 171,840 cells corresponding to 1,718,400 degrees of freedom and so it was slightly more refined that mesh M2 in the z-direction, but with fewer cells.

Since the aim here is the investigation of the appearance of velocity overshoots inside the smooth contraction, the following assessment of mesh convergence is based on velocity profiles in that region. Fig. 4(a) and (b) compares the spanwise and axial velocity profiles in the smooth contraction predicted with meshes M1 and M2 for the flow of PTT fluids with $We = 31.4$, $\varepsilon = 0.005$, $Re = 2.7$, $\xi = 0.2$ and $\beta = 1/11$. In the spanwise direction both meshes have the same number of cells and the differences in the velocity profiles are negligible, whereas in the cross-stream direction the results for the more refined mesh, M2, are slightly above those obtained with mesh M1. In Fig. 4(c) and (d) we compare predictions obtained with meshes M1 and M3 for a simulation where the velocity overshoots are stronger ($Re = 5.14$, $We = 47.1$, $\varepsilon = 0.005$, $\xi = 0.2$ and $\beta = 1/31$). Within the smooth contraction, the spanwise and cross-stream profiles of axial velocity are slightly different, but the main features we are looking at, the velocity overshoots, are present in both cases, even though to a less degree in the calculations with the coarse mesh. The use of the finer mesh enhances the appearance of velocity overshoots and moves them to the walls. An idea of the convergence in terms of stresses can be gained from inspection of Fig. 5, which compares contours of T_{xx} in the two centreplanes inside the smooth contraction and sudden expansion for the simulation in Fig. 4(a). The contours for mesh M1 are generally close to those pertaining to the finer mesh M2, especially near the re-entrant corner, showing that events in this region seem unrelated to the velocity overshoots. For the other stress components the differences between contours in both meshes are similar in magnitude. Given the extremely long time required to obtain converged solutions with meshes M2 and M3, most of the simulations where carried out using mesh M1. Even though there is a geometric singularity in the expansion, it does not affect events in the upstream smooth contraction as far as we could detect, and so this level of refinement is adequate for our purposes. Of course, extremely accurate predictions of viscoelastic stress in the vicinity of the singularity would require finer meshes having a minimum cell size at least one order of magnitude smaller. An idea of the degree of refinement required for such purposes by our calculation method, when using the Phan-Thien–Tanner model, and the corresponding accuracy of results, is presented in detail by Alves et al. [25]. It is also clear in [25] that accurate predictions of other quantities and elsewhere (meaning far from the geometric singularity) are not so demanding especially when involving constitutive equations with bounded properties as is the case of the PTT model.

All calculations were carried out on PC computers with AMD processors running at 3.0 GHz and typically each simulation took about 72, 216 and 180 h of CPU time to converge in meshes M1, M2 and M3, respectively.

3. Governing equations

The flow is assumed to be steady, laminar and the fluid is incompressible. The governing equations are those expressing conservation of mass:

$$\frac{\partial u_i}{\partial x_i} = 0 \tag{1}$$

and momentum:

$$\frac{\partial \rho u_i}{\partial t} + \frac{\partial \rho u_j u_i}{\partial x_j} = -\frac{\partial p}{\partial x_i} + \eta_s \frac{\partial^2 u_i}{\partial x_j \partial x_j} + \frac{\partial \tau_{ij}}{\partial x_j} \tag{2}$$

where u_i is the velocity vector, p the pressure, ρ the fluid density and the two last terms on the right-hand-side of Eq. (2) account for the contributions from the solvent and the polymer to the extra stress tensor, respectively.

The polymer contribution τ_{ij} is modeled by the PTT equation of Phan-Thien and Tanner [21] and Phan-Thien [22]:

$$f(\tau_{kk})\tau_{ij} + \lambda \left[\frac{\partial \tau_{ij}}{\partial t} + u_k \frac{\partial \tau_{ij}}{\partial x_k} - \tau_{jk} \frac{\partial u_i}{\partial x_k} - \tau_{ik} \frac{\partial u_j}{\partial x_k} + \xi(\tau_{ik} S_{kj} + S_{ik} \tau_{kj}) \right] = \eta_p \left(\frac{\partial u_i}{\partial x_j} + \frac{\partial u_j}{\partial x_i} \right) \tag{3}$$

The rate of deformation tensor S_{ij} is defined as $S_{ij} \equiv (1/2)((\partial u_i/\partial x_j) + (\partial u_j/\partial x_i))$ and the stress function $f(\tau_{kk})$ adopted here follows the linear form proposed in the original

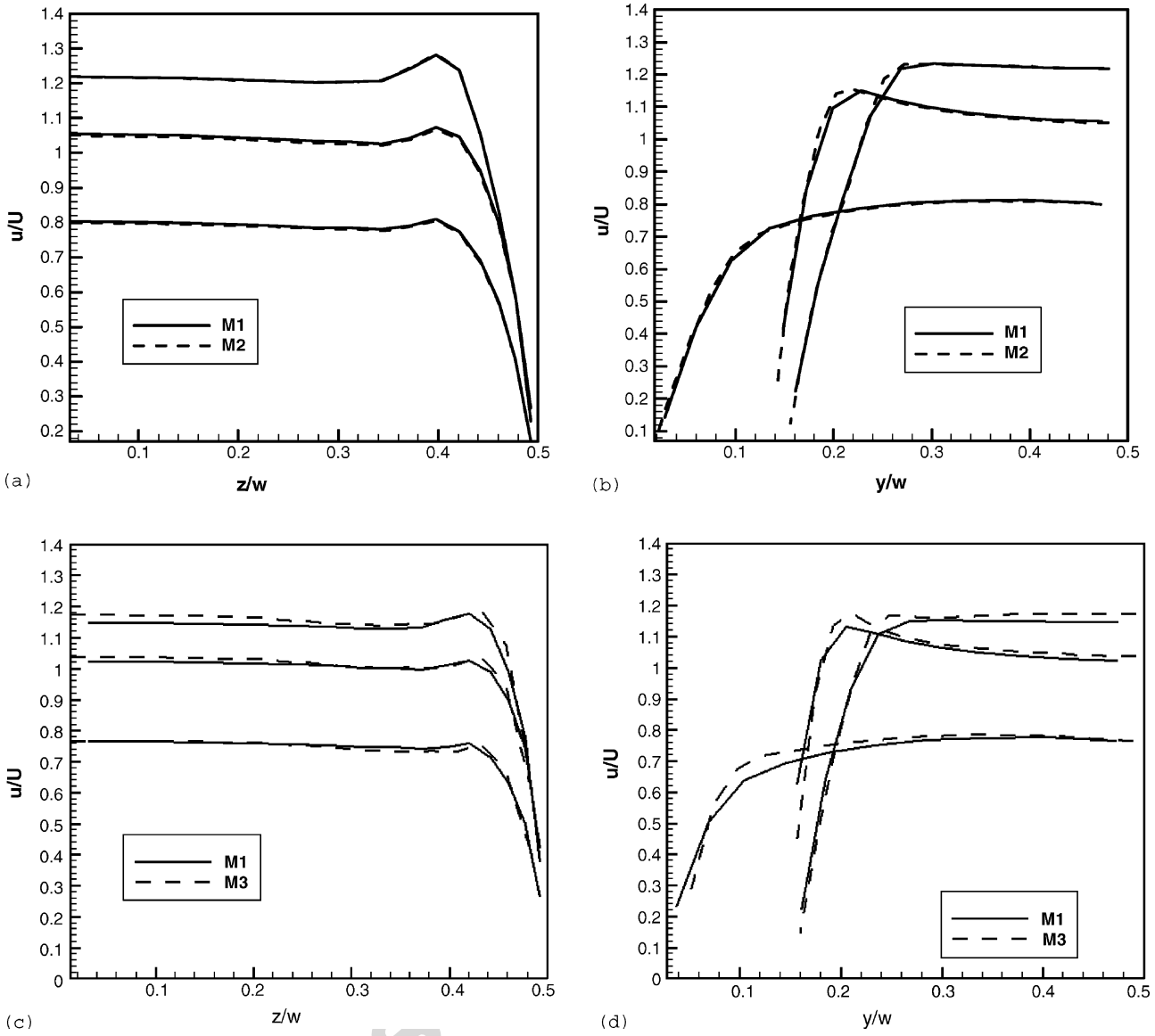

Fig. 4. Effect of mesh refinement on spanwise and transverse profiles of axial velocity in the smooth contraction. Profiles from bottom to top at $x/h = -4.0$, -2.06 and -0.1. (a) Spanwise and (b) transverse profiles for meshes Ml and M2 at $We = 31.4$, $\varepsilon = 0.005$, $Re = 2.7$, $\xi = 0.2$ and $\beta = 1/11$. (c) Spanwise and (d) transverse profiles for meshes Ml and M3 at $Re = 5.14$, $We = 47.1$, $\varepsilon = 0.005$, $\xi = 0.2$ and $\beta = 1/31$.

work of Phan-Thien and Tanner [21]:

$$f(\tau_{kk}) = 1 + \frac{\varepsilon\lambda}{\eta_p}\tau_{kk} \tag{4}$$

In Eqs. (2)–(4) the model parameters are the relaxation time of the polymer λ, the zero-shear polymer viscosity η_p, the Newtonian solvent viscosity η_S, the extensibility parameter ε and the slip parameter ξ. The slip parameter takes into account the non-affine motion between the polymer molecules and the continuum. The polymer strands embedded in the medium may slip with respect to the deformation of the macroscopic medium, thus each strand may transmit only a fraction of its tension to the surrounding continuum. When $\xi = 0$ there is no slip and the motion becomes affine. Parameter ξ is responsible for a non-zero second normal-stress difference in shear, leading to secondary flows in ducts having non-circular cross-sections, which is superimposed on the streamwise flow. The strength of the secondary flow depends on the values of both ξ, and the relaxation time λ.

The influence of all the constitutive parameters was investigated in this work, as part of relevant non-dimensional numbers, with the corresponding range of values listed in Table 1. These numbers are the Reynolds number, the Weissenberg number, ε,

Table 1
Range of the studied PTT parameters (non-dimensional form)

Parameters	Range
We	7.9–47.1
Re	0.4–5.1
Re_c	0.6–6.3
ε	0.001–0.25
ξ	0.001–0.2
β	1/31–1/11

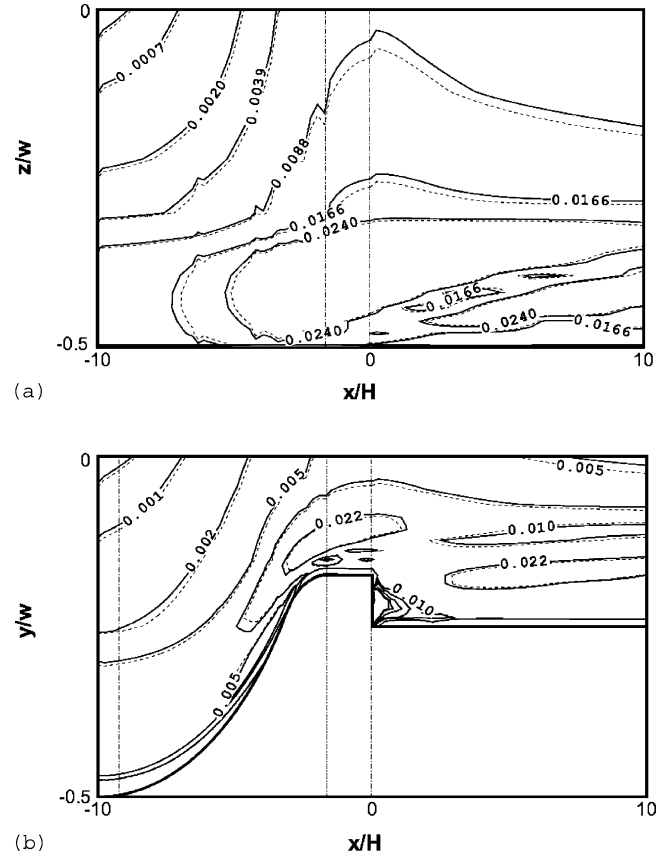

Fig. 5. Effect of mesh refinement on contours of T_{xx} in the smooth contraction and sudden expansion for meshes M1 (lines) and M2 (dashed) at $We = 31.4$, $\varepsilon = 0.005$, $Re = 2.7$, $\xi = 0.2$ and $\beta = 1/11$: (a) XZ-centreplane and (b) XY-centreplanes.

ξ and the viscosity ratio β defined as the ratio between the Newtonian solvent viscosity and the total zero shear rate viscosity η_0:

$$\beta \equiv \frac{\eta_s}{\eta_0} = \frac{\eta_s}{\eta_s + \eta_p} \tag{5}$$

The Reynolds number was defined on the basis of the total zero shear rate viscosity, the bulk velocity at the exit from the contraction U and for the length scale we selected the step height ($h = 0.006$ m):

$$Re = \frac{\rho U h}{\eta_0} \tag{6}$$

At a later stage in the paper, when analysing the effect of inertia, a second Reynolds number Re_c, based on a viscosity corresponding to a characteristic shear rate defined from bulk-flow quantities ($\dot{\gamma}_c = U/h$) is used. This second Reynolds number, defined in Eq. (7), is used by Poole et al. [1–3], and quantifies better the viscous forces within the shear layer downstream of the expansion:

$$Re_c = \frac{\rho U h}{\eta_c} \tag{7}$$

The Weissenberg number, We, is the ratio between the first normal-stress difference and the shear stress which is proportional to the product of the relaxation time of the fluid and a shear rate, here taken as the characteristic shear rate, $\dot{\gamma}_C$, at the backward facing step:

$$We = \frac{\lambda U}{h} = \lambda \dot{\gamma}_c \tag{8}$$

4. Numerical method

A fully implicit finite-volume method was used to solve Eqs. (1)–(3). The method is based on a time marching pressure–correction algorithm formulated with the collocated variable arrangement and is explained in detail in Oliveira et al. [26], Alves et al. [27,28]. Here, we briefly explain the method. The governing equations are transformed first to a non-orthogonal system ζ_1, but keeping the Cartesian velocity and stress components. This is advantageous from a numerical point of view because the equations are written in a strong conservation form which helps to ensure that the final algebraic equations retain conservativeness. Then, the equations are integrated in space over the control volumes (cells with volume V_P) forming the computational mesh, and in time over a time step (δt), so that sets of linearised algebraic equations are obtained, having the general form:

$$a_P u_P = \sum_{F=1}^{6} a_F u_F + S_U \tag{9}$$

to be solved for the velocity components, and

$$a_P^\tau \tau_P = \sum_{F=1}^{6} a_F^\tau \tau_F + S_\tau \tag{10}$$

to be solved for the polymeric contribution to the extra stress components. In these equations a_F are coefficients accounting for convection and diffusion, S are source terms encompassing all contributions not included in the coefficients, the subscript P denotes the cell under consideration and subscript F its corresponding neighbouring cells. The central coefficient of the momentum equation a_P is given by

$$a_P = \frac{\rho V_P}{\delta t} + \sum_{F=1}^{6} a_F \tag{11}$$

Similarly, the central coefficient of the stress equation for the linear PTT model is given by Eq. (12), where $\tau_{P,kk}$ denotes the trace of the stress tensor at cell P:

$$a_P^\tau = \frac{\lambda V_P}{\delta t} + V_P \left(1 + \frac{\lambda \varepsilon}{\eta_p} \tau_{P,kk}\right) + \sum_{F=1}^{6} a_F^\tau \tag{12}$$

For this work, it was necessary to extend the method to the full PTT model and this required only the addition of the new terms in Eq. (3), related to parameter ξ. In the algebraic equation (10) they contribute to the total source term S_τ and are denoted by $S_{\tau\xi}$ which, after discretization, is given by Eq. (13) for stress

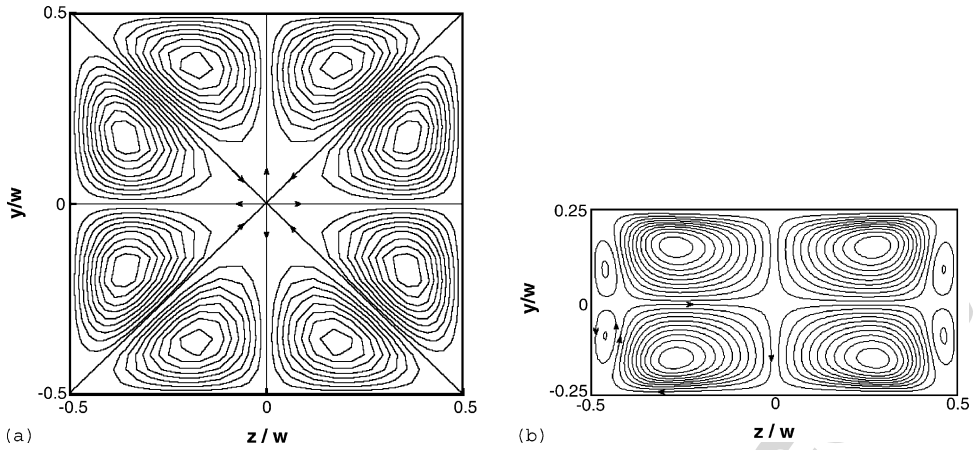

Fig. 6. Simulated secondary-flow cross-stream ($\xi = 0.2$) at: (a) $x/h = -70$ and (b) at $x/h = 120$. Streamlines are plotted at equally spaced increments between: (a) -2.85×10^{-5} and 2.85×10^{-5}; (b) -6.0×10^{-2} and 6×10^{-2}.

component τ_{ij}:

$$S_{\tau\xi} = -\frac{\lambda\xi}{2}\left(\beta_{lk}\tau_{kj}\frac{\partial u_i}{\partial\zeta_l} + \beta_{lk}\tau_{ki}\frac{\partial u_j}{\partial\zeta_l} + (\beta_{li}\tau_{kj} + \beta_{lj}\tau_{ki})\frac{\partial u_k}{\partial\zeta_l}\right) \tag{13}$$

where ζ_l are the components of the general non-orthogonal coordinate system and β_{li} are metric coefficients defined as the cofactor of $\partial x_i/\partial\zeta_l$ and readily interpreted as area components after integration. The first derivatives of the velocity in Eq. (13) were calculated with high-resolution scheme CUBISTA of Alves et al. [28]. The boundary conditions for the velocity and stress followed the previous work [26–28], whereas the pressure at the wall was extrapolated from the domain according to Oliveira [29].

After assembling all coefficients and source terms, the linear sets of Eq. (9) are solved sequentially for the three Cartesian velocity components u, v and w. These newly computed velocity components do not, in general, satisfy the continuity equation and need to be corrected by an adjustment of the pressure differences which drive them. This adjustment is accomplished by means of a pressure-correction field obtained from a Poisson pressure equation, derived from the discretised equivalent of Eq. (1) and a simplified form of Eq. (9), which is then solved with a symmetric conjugate gradient method preconditioned with an incomplete LU decomposition. Once a velocity field satisfying continuity has been obtained, the implicitly discretised constitutive equations for the polymeric contribution to the extra stress components (i.e. Eq. (10)) are solved sequentially. Full details are given in [26].

To formulate the convective fluxes, the code uses the high-resolution scheme CUBISTA, formally of second-order accuracy and especially designed for differential constitutive relations (see [28]). The scheme has the advantage over more classical schemes (e.g. the SMART scheme of Gaskell and Lau [30]) of promoting iterative convergence when employed in conjunction with implicit methods.

5. Results and discussion

In this section, the results of the numerical simulations are presented and discussed. Since our primary interest is the investigation of the conditions for the appearance of velocity overshoots near the walls, the results focus on the contraction region. All simulated cases were analyzed and separated into those that exhibited velocity overshoots and those that did not. Comparisons between simulations are made with spanwise and transverse profiles of the streamwise velocity in the *XZ*- and *XY*-centreplanes, within and outside the smooth contraction (specifically at $x/h = -8.0$, -4.0, -2.06 and -0.1), but only relevant profiles are shown below.

5.1. Effect of second normal-stress difference (parameter ξ)

The fully developed flow through a non-circular duct of fluids with a non-zero second normal-stress difference ($\xi \neq 0$ for the PTT model) is characterized by a secondary flow in the cross-section which is superimposed on the streamwise flow. The secondary flow arises as a consequence of an imbalance of normal stresses in the cross-section plane and bears some resemblances to events for turbulent flow of Newtonian fluids in non-circular ducts [24,31], although for Newtonian turbulent flows the secondary motion is stronger than and its sense of rotation opposite to that for the laminar flow of viscoelastic fluids for equal streamwise flow strengths. In the laminar regime the secondary flow does not exist for fluids or models exhibiting a zero second normal-stress difference in shear, such as fluids obeying the generalized Newtonian and the PTT (with $\xi = 0$) constitutive equations. For square ducts, the secondary motion in fully developed laminar flow of viscoelastic fluids was first investigated numerically by Wheeler and Whissler [32] and Townsend et al. [33], both numerically and experimentally. More recently, Gervang and Larsen [34], Debbaut et al. [35] and Siline and Leonov [36] showed that the magnitude of the secondary-flow velocities are typically two orders of magnitude lower than that of the streamwise velocity (the secondary motion actually varies with the fourth power of the axial velocity at low shear rates and

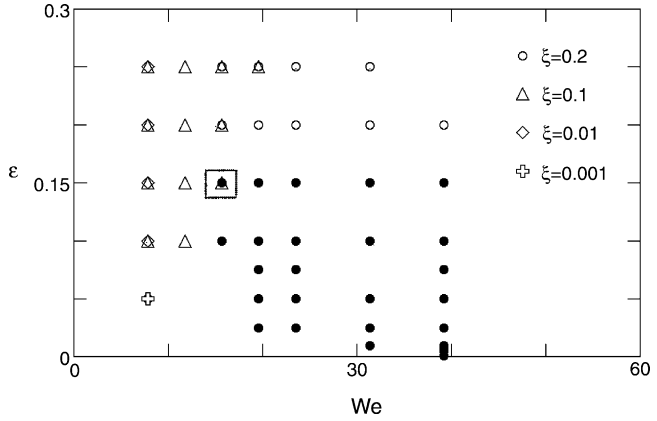

Fig. 7. Maps of simulations for $Re = 5.14$ and $\beta = 1/11$ as function of ε, We and ξ. Velocity overshoots were found in velocity profiles for the simulations represented by filled symbols in the XZ-centreplane.

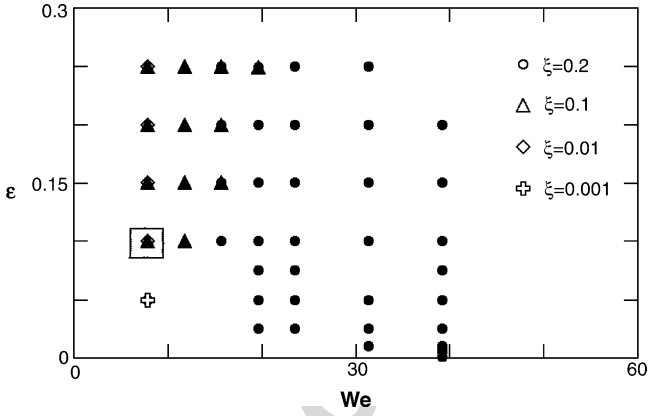

Fig. 9. Map of simulations for $Re = 5.14$ and $\beta = 1/11$ as function of ε, We and ξ. Velocity overshoots were found in velocity profiles for the simulations represented by filled symbols in the XY-centreplane.

linearly with the axial velocity at high shear rates according to Refs. [35,36]).

The strength of the secondary flow depends on the values of both ξ and the Weissenberg number and in Fig. 6 we show the streamlines for the secondary flow corresponding to a simulation with a high value of ξ ($\xi = 0.2$, $\varepsilon = 0.05$, $We = 7.93$, $Re = 5.14$ and $\beta = 1/11$). The stream-function is normalized by the streamwise flow rate and the plots are at a location well upstream of the inlet of the contraction ($x/h = -70$, Fig. 6(a)) and in the duct outlet ($x/h = 120$, Fig. 6(b)). The patterns of the secondary flow are symmetric about the diagonal and the two mid-planes in the inlet square duct ($x/h = -70$), whereas increasing aspect ratio expands the vortices near the top and bottom walls while squeezing them near the side walls ($x/h = 120$). Nevertheless, in all cases there are eight vortices as expected [18,36,37].

In the fully developed flow region, at the inlet square duct, the maximum secondary-flow velocities are close to 0.0002 m/s for maximum streamwise velocities of about 0.32 m/s, i.e. the streamwise flow is three orders of magnitude stronger than the secondary flow. Similar results were obtained by Gervang and Larsen [34] using the modified PTT model (MPTT) and Debbaut et al. [35] with a Giesekus model, although the latter found

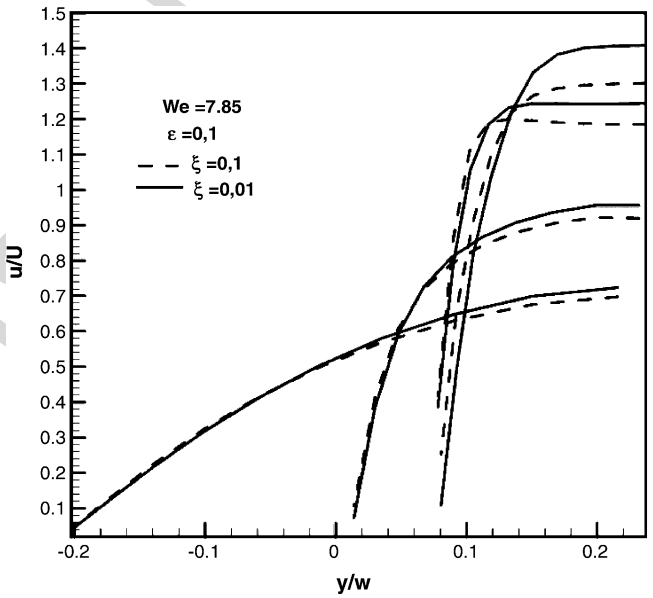

Fig. 10. Transverse profiles of streamwise velocity inside the smooth contraction: $We = 7.85$, $\varepsilon = 0.1$, $Re = 5.14$ and $\beta = 1/11$ (profile location as in Fig. 8).

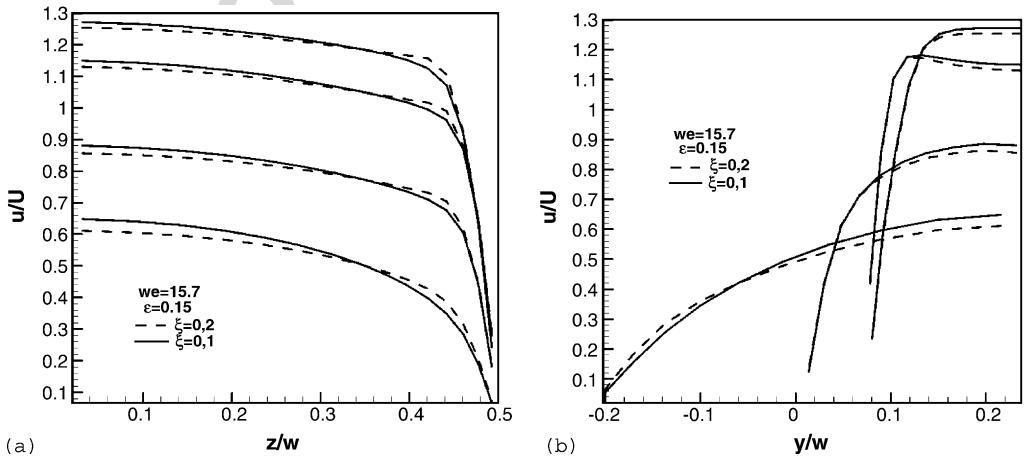

Fig. 8. Spanwise (a) and transverse (b) profiles of streamwise velocity in the smooth contraction: $We = 15.7$, $\varepsilon = 0.15$, $Re = 5.14$ and $\beta = 1/11$ (profiles from bottom to top at $x/h = -8.0$, -4.0, -2.06 and -0.1).

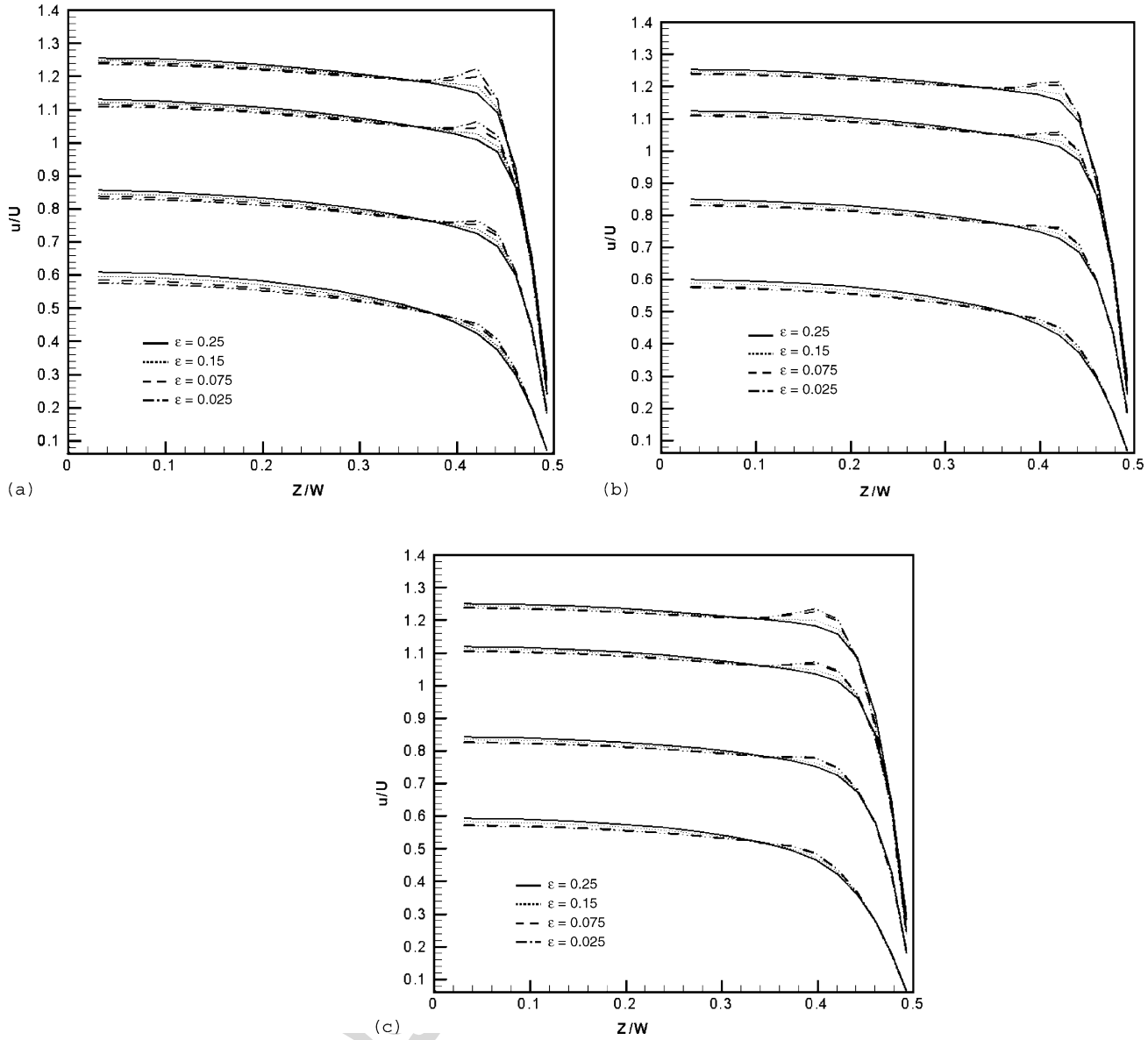

Fig. 11. Effect of ε on development of velocity profiles within contraction for $y/w = 0$ (XZ-centreplane) at $Re = 5.14$, $\xi = 0.2$ and $\beta = 1/11$. Profile location as in Fig. 8: (a) $We = 19.6$, (b) $We = 23.5$ and (c) $We = 31.4$.

a stronger secondary flow, with its velocity components in the cross-section plane only two orders of magnitude lower than the axial velocity. These differences relate to the different dependencies of the secondary motion on the axial velocity at low and high shear rates, mentioned above. Decreasing the value of ξ to 0.001, but keeping all other parameters unchanged, weakens the secondary flow leading to maximum cross-stream velocities of the order of 1 μm/s while the maximum streamwise velocity remains essentially unchanged. Since the secondary flow is much weaker than the streamwise flow, the shear viscosity is basically determined by the latter.

At this stage it is worth commenting that in pure shear flow, for the full PTT model $\tau_{xx} \propto 1/\xi$ and $\tau_{yy} = -\xi\tau_{xx}/(2-\xi)$ [38], hence an increase in ξ reduces N_1 in proportion and mildly increases N_2. The flow, however, is proportional to the local gradients of the individual stresses, which are more affected by the variations in ξ.

Fig. 7 presents an ε–We map of the simulations that were carried out for several values of ξ ($\xi = 0.001$, $\xi = 0.01$, $\xi = 0.1$ and $\xi = 0.2$), at a constant Reynolds number Re of 5.14 and a constant viscosity ratio β of 1/11. The initial simulations to predict the measured flows [3] lead to this particular value of the zero shear rate Reynolds number (Re). The closed symbols represent those cases where velocity overshoots were observed in the XZ-centreplane velocity profiles and the symbols marked with an outer square pertain to simulations represented in Fig. 8 (with and without velocity overshoots). As shown here, for $Re = 5.14$ velocity overshoots were found only in simulations for $\xi = 0.2$, at high Weissenberg numbers and low values of ε. These conditions correspond to fluids with high steady and transient extensional viscosities ($\varepsilon = 0$ gives an unbounded steady extensional viscosity) and large second normal-stress differences (high values of ξ). Values of ξ, higher than 0.2 lead to convergence difficulties, presumably because of the non-monotonic nature of the shear

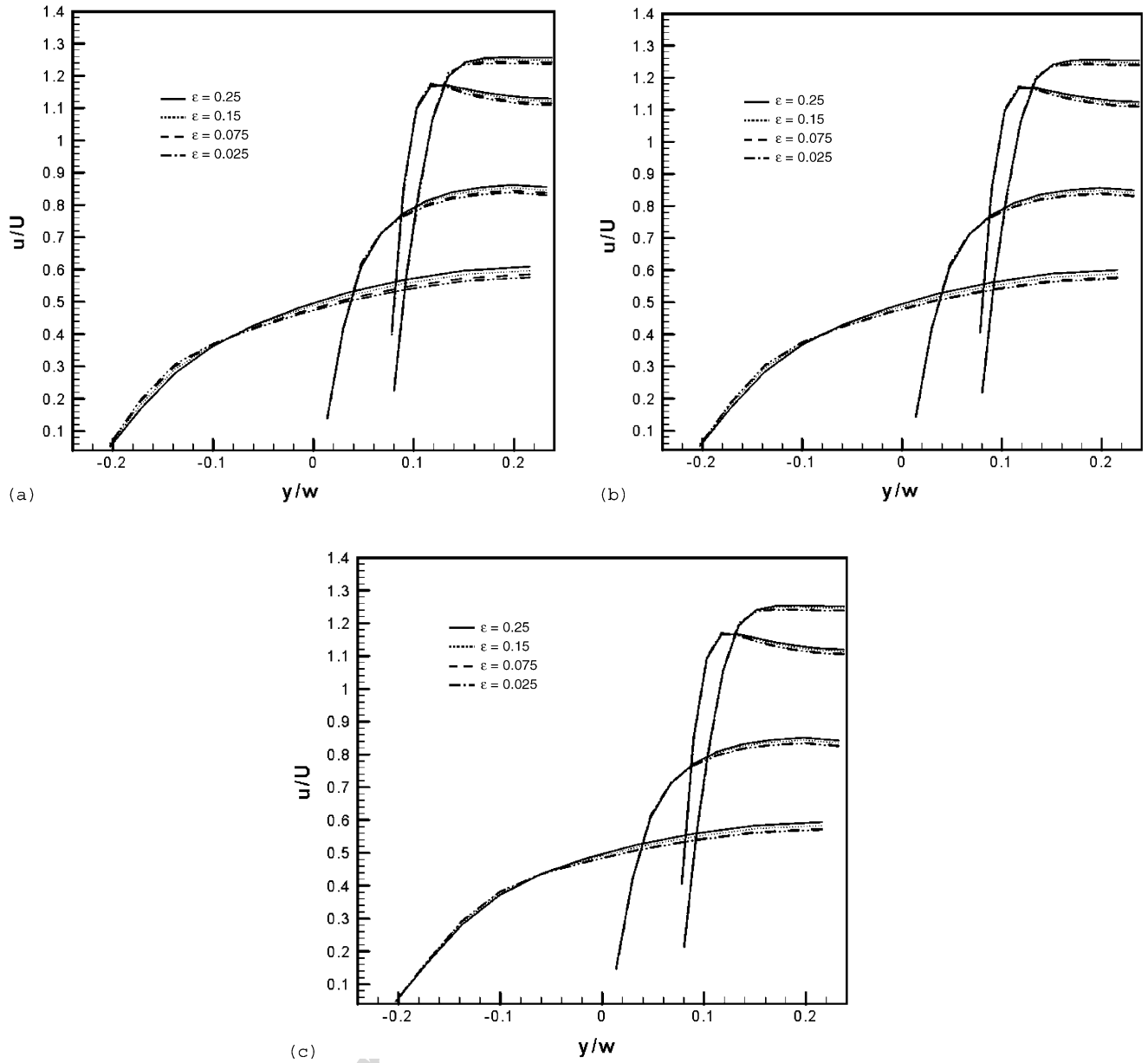

Fig. 12. Effect of ε on development of velocity profiles within contraction for $z/w = 0$ (*XY*-centreplane) at $Re = 5.14$, $\xi = 0.2$ and $\beta = 1/11$. Profile location as in Fig. 8: (a) $We = 19.6$, (b) $We = 23.5$ and (c) $We = 31.4$.

stress/shear rate relation [39]. In any case values of $|N_2/N_1|$ rarely exceed 0.2 and more often are of the order of 0.1, which for the PTT model is obtained when $\xi = 0.2$.

In Fig. 8 profiles of the streamwise velocity in the two mid-planes are compared for different values of ξ, all other parameters being equal ($\varepsilon = 0.15$, $We = 15.7$). Both cases show a small velocity overshoot in the *XY*-centreplane, but only for $\xi = 0.2$ there is a velocity overshoot near the end of the contraction, in the *XZ*-direction. This clearly shows that a high value of ξ is required for the appearance of velocity overshoots, especially when the extensional viscosity is low (high value of ε). For lower values of ε, the effect of ξ becomes more pronounced, as will be shown later. The flow inside the contraction is extensional except near the walls where shear is also important. So, the fluid particles undergo a transient of limited duration and the transient extensional viscosity rather than the steady extensional viscosity is the relevant property. In any case, the variation of ε affects both extensional viscosities in the same way.

The magnitude of the slip factor (ξ) also affects the appearance of overshoots in the velocity profiles at the *XY*-centreplane. These overshoots are different from and weaker than those occurring on the flat sidewalls and have not been reported by Poole et al. [3]. Fig. 9 shows again the ε–*We* map of simulations of Fig. 7, but now illustrating the cases for which there were velocity overshoots in the *XY*-centreplane. Comparing the maps of Figs. 7 and 9, it is obvious that velocity overshoots on curved walls are more frequent than on flat surfaces and only the simulations with lower values of ξ ($\xi \leq 0.01$) do not show the overshoots on the curved walls. For the simulations marked with an outer square in Fig. 9, velocity profiles on the *XY*-centreplane

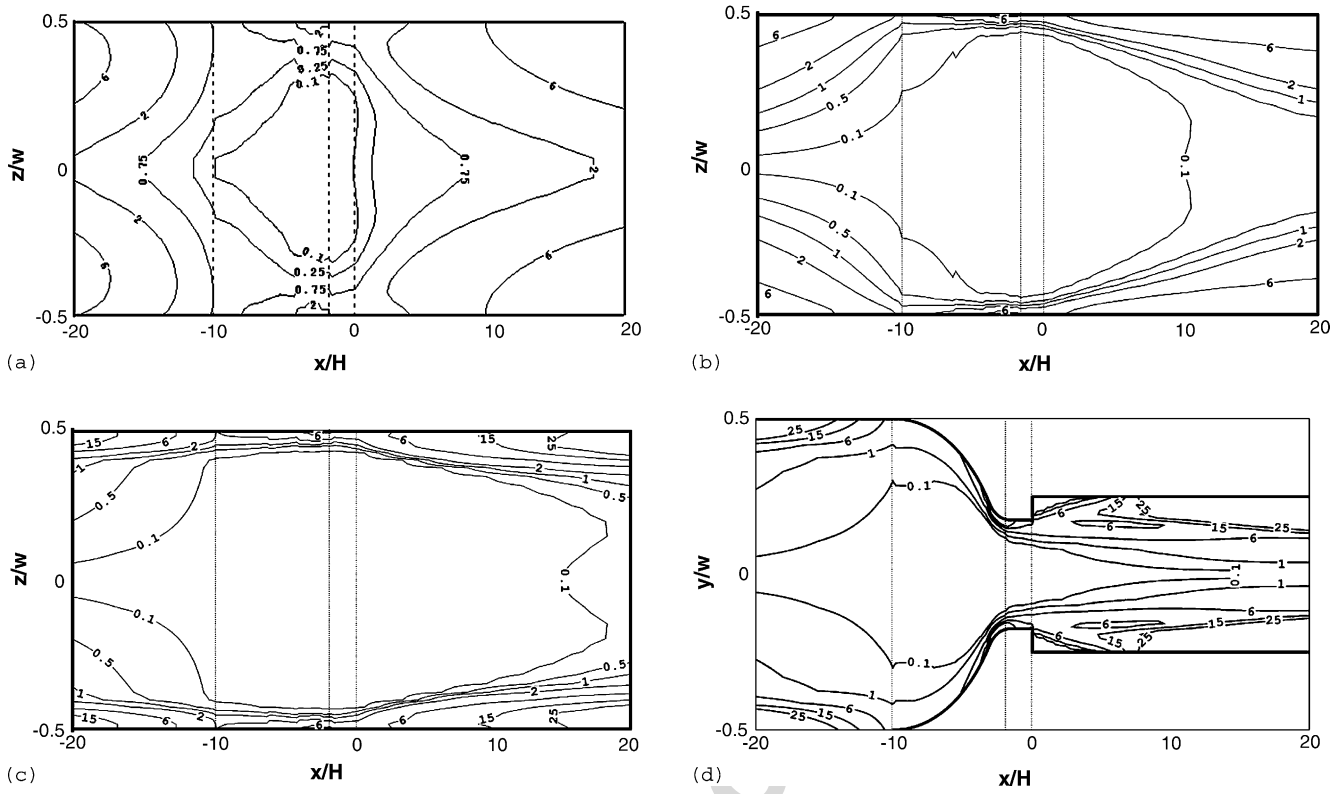

Fig. 13. Contour maps of the normalised enstrophy ($\omega^2/(U^2/h^2) \times 10^{17}$) in the contraction and its vicinity for the *XZ*- and *XY*-centreplanes at $Re = 5.14$ and $\beta = 1/11$: (a) $\xi = 0$, $We = 7.85$, $\varepsilon = 0.05$; (b) $\xi = 0.1$, $We = 19.6$, $\varepsilon = 0.25$; (c and d) $\xi = 0.2$, $We = 19.6$, $\varepsilon = 0.025$.

are shown in Fig. 10: one set of curves pertains to a flow exhibiting overshoots ($\xi = 0.1$), whereas the other set pertains to a case without velocity overshoots in the curved walls ($\xi = 0.01$), all other parameters being equal. These two cases have $We = 7.85$, lower than in Fig. 8.

In conclusion, the main velocity overshoots are near the walls on the *XZ*-centreplane and in this geometry these were not observed when the secondary motion is weak (meaning $\xi \leq 0.1$), within the ranges tested for all parameters (see Table 1). Very recently, Alves [40] has observed velocity overshoots in preliminary calculations of the flow of an upper convected Maxwell model inside a stronger smooth contraction (his contraction ratio was equal to 8:1) following a square duct and without the downstream expansion. In our geometry, having a smaller contraction of 2.86:1, we could not observe velocity overshoots in converged solutions for $\xi = 0$ and $\varepsilon = 0$, which were also limited to rather low values of the Weissenberg number. To obtain converged solutions at higher Weissenberg numbers we had to limit the stresses ($\varepsilon \neq 0$) and to observe velocity overshoots large values of ξ were needed. So, it looks as though a non-zero value of ξ may not be required to observe velocity overshoots when the smooth contraction has a larger ratio, whereas in our smaller contraction $\xi \neq 0$ was essential to see this phenomenon. However, the clarification of this issue requires further research with different contractions, and probably also with different constitutive equations since the very intense peaks measured by Poole et al. [3] in this geometry, much stronger than the results of any of the calculations presented here, suggest that something is being missed by this constitutive model.

5.2. Effects of extensional viscosity and Weissenberg number

The effect of extensional viscosity on the existence of velocity overshoots can be assessed by looking at simulations at a constant Weissenberg number (vertical lines) in Figs. 7 and 9. These simulations have the same zero shear rate Reynolds number *Re* of 5.14, $\beta = 1/11$ and a constant value of $\xi = 0.2$ for which the velocity overshoots were more pronounced. In Figs. 11 and 12 profiles of the streamwise velocity in the *XZ*- and *XY*-centreplanes, respectively, are plotted as function of ε at various x/h locations from the beginning to the end of the contraction. In each figure three different Weissenberg numbers are considered.

The velocity profiles across the spanwise direction in Fig. 11 are particularly clarifying. Velocity overshoots start to develop inside the contraction (there are already signs at $x/h = -4.0$) and increase even after the end of the contraction (the contraction ends at $x/h = -1.66$ and the overshoots at $x/h = -0.1$ are larger than at $x/h = -2.06$). The effect is enhanced as ε decreases regardless of the Weissenberg number. When $\varepsilon = 0.25$, for which the strain-hardening of the extensional viscosity is very mild, no velocity overshoots are observed (see also Fig. 7). Comparing Fig. 11(a)–(c) there is also broadening of the velocity peaks and their progressive movement away from the flat wall and towards the centreplane as the Weissenberg number increases. The effect of ε seems stronger at low Weissenberg numbers because of the narrower peaks. The velocity overshoots become especially sensitive to ε as this quantity tends to zero, since this corresponds to a large increase in the transient extensional vis-

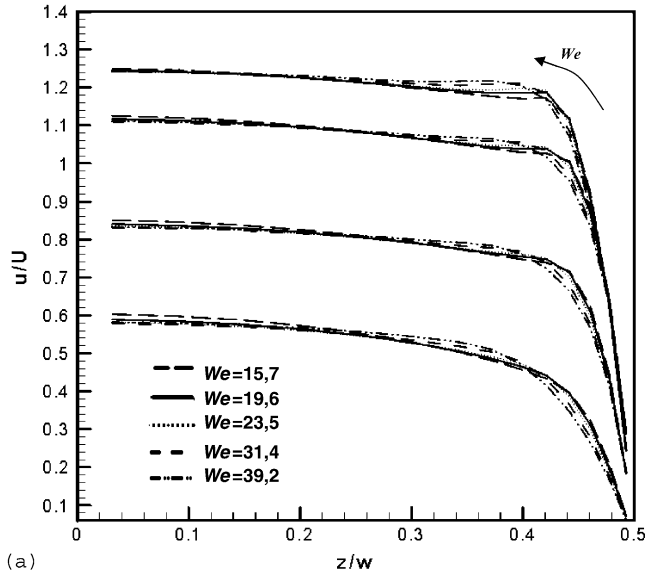

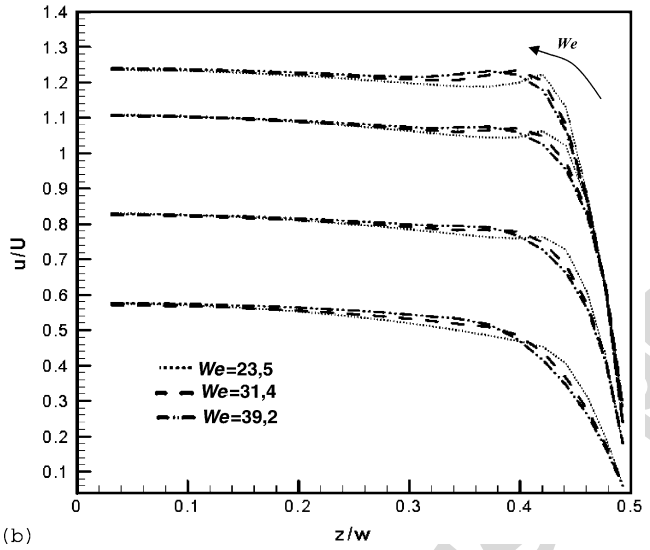

Fig. 14. Spanwise and axial velocity profiles in the smooth contraction for different We number, $Re = 5.14$, $\xi = 0.2$ and $\beta = 1/11$. Profile location as in Fig. 8: (a) $\varepsilon = 0.1$ and (b) $\varepsilon = 0.025$.

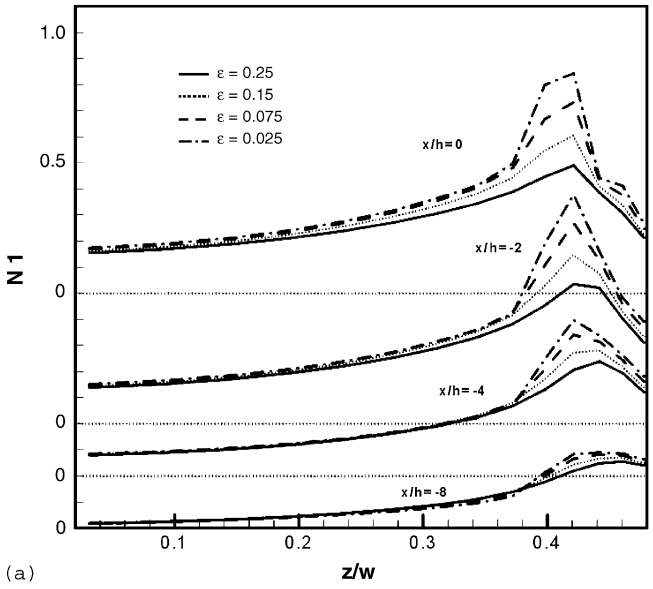

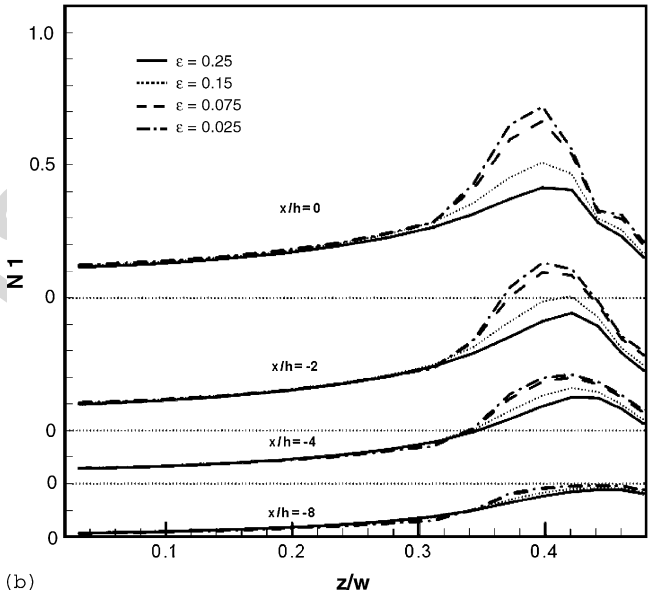

Fig. 15. Effect of ε on the N_1 within the contraction for $y/w = 0$ (XZ-centreplane) at $Re = 5.14$, $\xi = 0.2$ and $\beta = 1/11$: (a) $We = 19.6$ and (b) $We = 31.4$.

cosity ($\varepsilon = 0$ corresponds to an unbounded steady extensional viscosity). Since $\xi \neq 0$ and $\beta < 1/9$ it may also be argued that the overshoots are a consequence of the non-monotonic shear stress/shear rate behaviour of this constitutive model. As we show later in Section 5.3 (in Fig. 17), velocity overshoots are also seen for $\beta > 1/9$ thus showing that this is unrelated to the non-monotonic shear stress/shear rate steady behaviour of the PTT model discussed in detail by Georgiou and Vlassopoulos [39].

Another likely cause, actually suggested by one of the reviewers, is the oscillating response of transient properties of the PTT fluid to a change of flow kinematics. Plots of stresses along stream traces did sometimes oscillate, but since these were seen where the cell size variation was less regular and the mesh is not very fine, it was not clear whether this was a genuine oscillation or a numerical artifact. More refined meshes are required to determine whether there is a possible link between the velocity overshoots and the transient behaviour of the fluids.

The velocity profiles in the XY-centreplane are much less sensitive to ε and Weissenberg number. Here, the velocity overshoots are only seen inside the contraction, as shown at $x/h = -2.06$, and are absent at the end of the contraction and beyond. Nevertheless, a small increase in the velocity overshoot is noticed when ε decreases due to lower velocities on the centreplane region. From Fig. 12, and the observations in Section 5.1, it seems that the velocity overshoots near the curved wall result from the combined effects of Reynolds number and flow contraction with a small influence of fluid rheology.

Unexpected phenomena in viscoelastic flows are often associated with a change of type of the equations, which lead to a dramatic change in the behaviour of the vorticity field within the

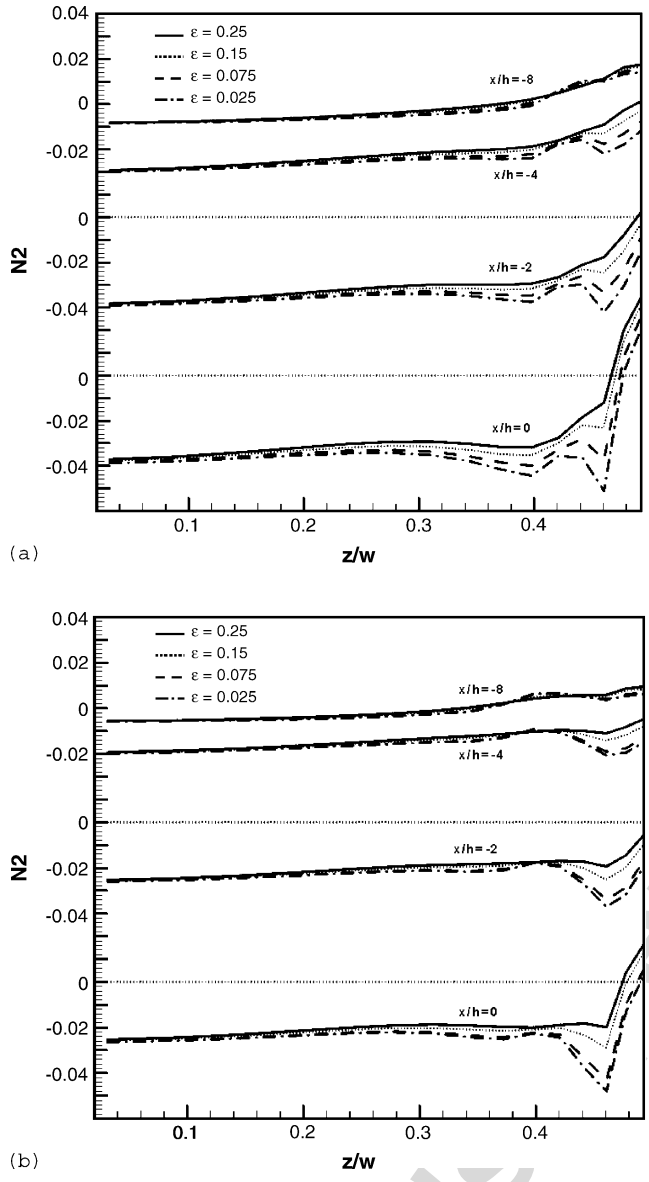

Fig. 16. Effect of ε on the N_2 within the contraction for $y/w = 0$ (XZ-centreplane) at $Re = 5.14$, $\xi = 0.2$ and $\beta = 1/11$: (a) $We = 19.6$ and (b) $We = 31.4$.

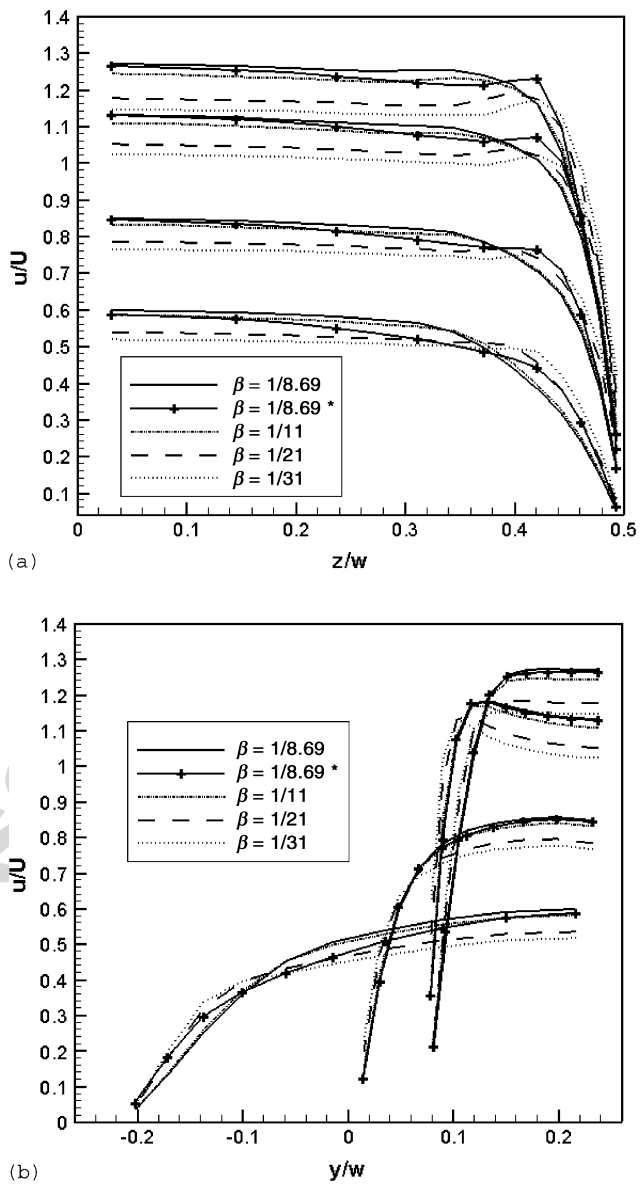

Fig. 17. Spanwise and cross-stream profiles of streamwise velocity in the smooth contraction: $Re = 5.14$, $We = 47.1$, $\varepsilon = 0.005$, $\xi = 0.2$ and different β (profile location as in Fig. 8). Data marked with asterisks (*) refers to $We = 19.6$.

flow domain [41,42] when the local flow velocity exceeds the local wave speed of elastic shear waves. This is seen as regions of very low vorticity bounded by regions of sharp gradients. Here, the equations are elliptic and do not change type because of the Newtonian solvent contribution, even though its viscosity is small. Nevertheless, given the small solvent viscosity, the polymer contribution is strong and the flow may exhibit characteristics typical of supercritical flows. Therefore, we present in Fig. 13 contour maps of the enstrophy ($\omega^2 \equiv \vec{\omega} \cdot \vec{\omega}$ where the vorticity vector is given by $\vec{\omega} = \text{curl}\, \vec{U}$) for three different flow conditions: $\xi = 0$, $\xi \neq 0$ without and with velocity overshoots. Three contour plots of ω^2 are in the XZ-centreplane and one is in the XY-centreplane, the flow is from left to right and the three vertical dashed lines mark the inlet and outlet of the contraction and the beginning of the expansion, respectively.

Starting with the XZ maps, when $\xi = 0$ and there are no velocity overshoots (Fig. 13(a)) the "region of low enstrophy" is very small and confined to the core of the contraction. The flow in Fig. 13(b) has $\xi = 0.1$, $We = 19.6$ and $\varepsilon = 0.25$ and shows no velocity peaks (cf. Fig. 7). The region of low enstrophy is now much longer and wider, extending further downstream into the exit duct. In the first half of the contraction this region of $\omega^2 \approx 0$ does not go up to the wall, i.e. the steep gradient near the wall is found only at the end of the contraction. In contrast, when we observe velocity peaks, such as for the case in Fig. 13(c), the "region of silence" inside the contraction extends to the side flat walls along the full length of the contraction, thus creating a long region of steep vorticity gradient. The velocity peaks are found at the inner edge of this vorticity boundary layer. Finally, looking at the corresponding contour plot in the XY-centreplane for this case in Fig. 13(d), we understand why velocity peaks are so difficult to observe in the cross-stream profiles. Here, the

region of steep enstrophy gradients is really limited to the final part of the contraction. Contour maps of enstrophy in the *XY*-centreplane (not shown here) are not too different from each other.

To better assess the effects of Weissenberg number, velocity profiles pertaining to a constant value of ε are compared in Fig. 14. The data correspond to horizontal lines in the maps of Fig. 7 (or Fig. 9), but only those with $\xi = 0.2$ and $Re = 5.14$ were selected.

The profiles of the streamwise velocity on the XZ-centreplane plotted in Fig. 14 show better the broadening of the velocity overshoots and their displacement towards the centreplane as the Weissenberg number increases. The influence of *We* is stronger at intermediate values of ε ($\varepsilon = 0.1$), and as the peak broadens its intensity remains basically the same (at fixed ε and ξ). More simulations at lower values of *We* ($We \leq 15.7$), together with lower values of ε ($\varepsilon \leq 0.1$), are required to show better this effect, but these were cases exhibiting convergence difficulties.

The effects of ε and *We* on the spanwise profiles of N_1 and N_2 are shown in Figs. 15 and 16, which correspond to some of the velocity profiles in Fig. 11(a) and (c). In Fig. 15 very large peaks of N_1 are observed in the region of the velocity overshoots, which grow as ε decreases. As the fluid progresses along the contraction there is also a general increase in N_1 due to the extensional flow and which is marginally larger in the core of the contraction as ε decreases. The increase in N_1 in the velocity overshoot region is disproportionately larger than elsewhere. The shear properties of N_1 for the PTT model (Fig. 2 in [38]) shows that N_1 is quadratic at low shear rates, constant at high shear rates and exhibits a mild dependence on ε at intermediate rates. These properties do not justify the large increase of N_1 in the velocity overshoot region seen in Fig. 15 as ε decreases because the peak N_1 is not found at the wall where shear rates are largest, but in a region of lower shear rates (cf. Fig. 11 to check that there is even a local minimum in shear rate). Therefore, the remaining contribution to N_1 must come from extension even though at the centre of the duct the effect of extension on N_1 is weaker. The broadening of the velocity overshoots region, due to an increase in the Weissenberg number, has a corresponding impact on the broadening of the peaks in N_1 shown in the comparison between Fig. 15(a) and (b). This broadening of the peak of N_1 is accompanied by a decrease in N_1 as happens also with the velocity overshoots in Fig. 11. No profiles of N_1 are presented here for a flow case without velocity overshoots, in which case N_1 increases towards the wall due to its dependence on the shear rate [38], and exhibits accordingly a decrease with ξ.

The corresponding behaviour of N_2 in Fig. 16 is more complex. As for N_1 the profiles are not very sensitive to ε between the centreplane and the velocity overshoot region. As this region is approached, N_2 exhibits strong spatial variations, which increase in magnitude along the contraction. Whereas at low *We* numbers the profiles show two negative peaks of similar magnitudes, followed by an increase of N_2 to positive values at the wall, the profiles at higher We show a small and a large negative peak before the increase near the wall. These strong oscillations of N_2 certainly help create large stress gradients, which are the driving forces of flows and are likely responsible for the appearance of the velocity overshoots. As already mentioned, for this contraction we were unable to observe velocity overshoots in the absence of N_2 or when N_2 was too small. Again, there could be a link between these large spatial gradients, the oscillating behaviour of transient properties and the appearance of velocity overshoots, but these require further investigation.

5.3. Effect of shear-thinning intensity

The influence of the viscosity ratio, and hence of shear-thinning, was also investigated and revealed interesting features. In all simulations so far the viscosity ratio was kept constant at $\beta = 1/11$. Increasing the zero-shear polymer viscosity (decreas-

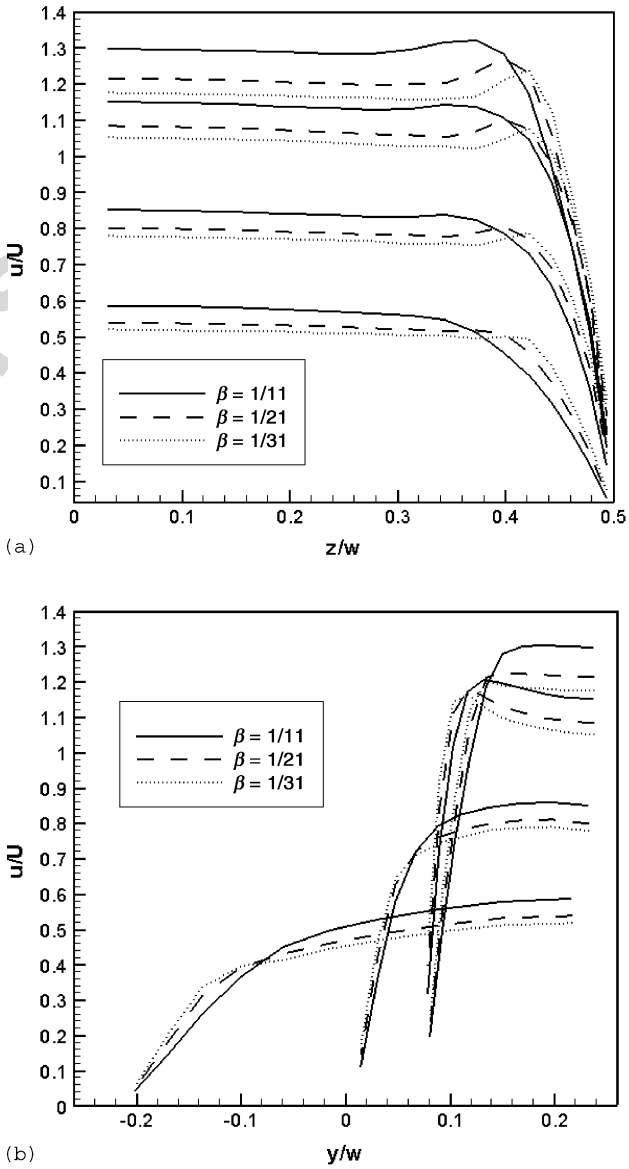

Fig. 18. Spanwise and cross-stream profiles of streamwise velocity in the smooth contraction: $Re = 2.84$, $We = 47.1$, $\varepsilon = 0.005$, $\xi = 0.2$ and different β (profile location as in Fig. 8).

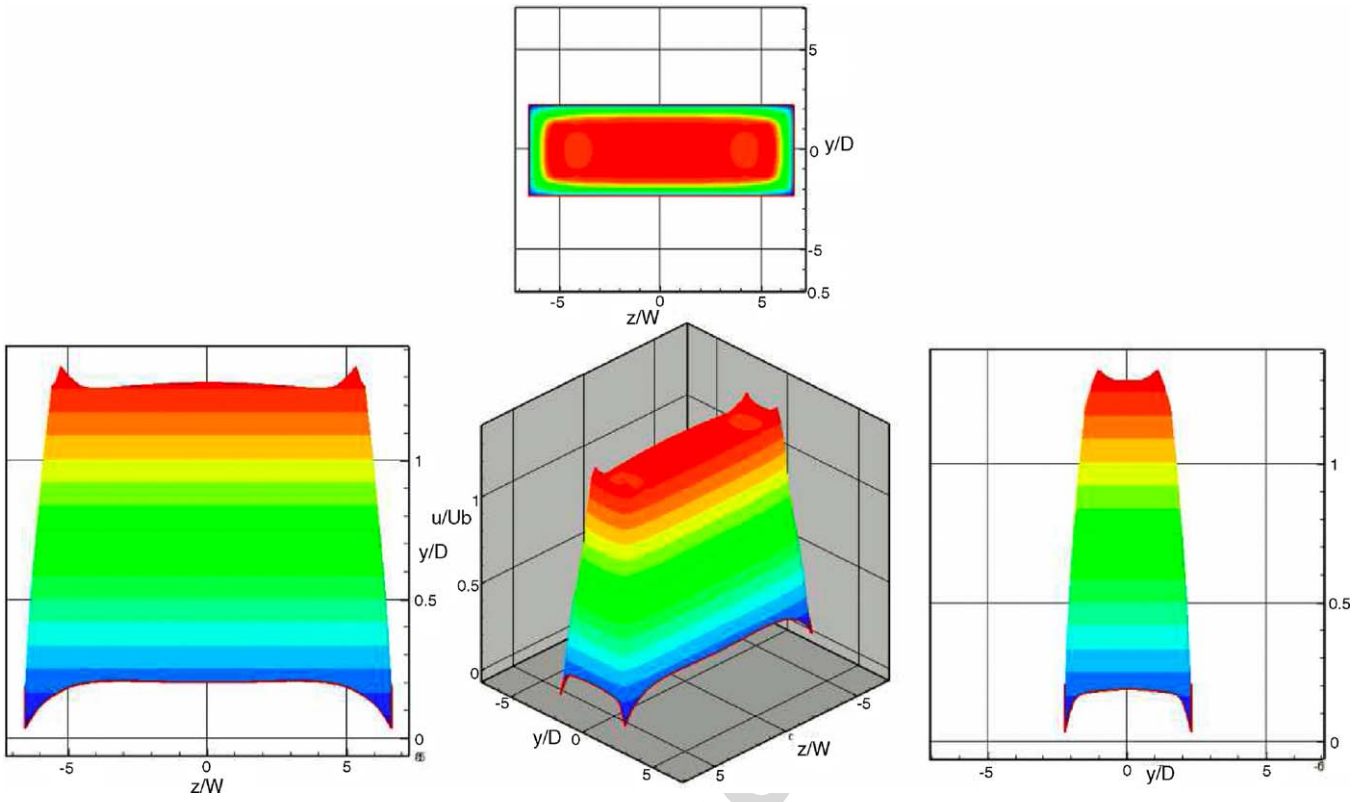

Fig. 19. 3D profiles in the smooth contraction at $x/h = -0.1$ for $We = 21.6$, $Re = 3.5$, $\xi = 0.2$, $\varepsilon = 0.005$ and $\beta = 1/11$.

ing the viscosity ratio β), at a constant Reynolds number, is seen to enhance the appearance of velocity overshoots as can be seen in Fig. 17(a), where spanwise profiles of the streamwise velocity are plotted as a function of β for $Re = 5.14$, $We = 47.1$, $\varepsilon = 0.005$ and $\xi = 0.2$. For lower values of β the velocity overshoots in the XZ-centreplane develop earlier inside the contraction than in the previous simulations (there are already signs of the overshoots at $x/h = -8.0$) and tend to be stronger. Similarly, the velocity profiles in the XY-centreplane, plotted in Fig. 17(b), show more pronounced velocity peaks as β is reduced, and the weak velocity overshoots in this plane are now enhanced. Simultaneously, decreases in velocity at the centre of the duct are observed in both plots to conserve mass. The figures include also data for a higher value of β ($\beta > 1/9$) in order to assess whether the loss of monotonicity of the shear stress/shear rate of the PTT model is the cause for the velocity overshoots. The velocity overshoots are still present and to make this clear data for a different value of We is presented, for which the peaks are stronger. Thus, we may conclude that the loss of monotonicity is unrelated to the appearance of velocity peaks, although it may help to enhance it when β is reduced.

Reducing the Reynolds number to 2.84, while maintaining all other parameters unchanged, leads to a stronger effect of β as seen in the centreplane velocity profiles of Fig. 18(a) and (b). The flow features are qualitatively the same as in Fig. 17, but more intense effects are observed in the sense that the velocity overshoots become more localized and move closer to the wall, which is especially noticeable after the end of the contraction, at $x/h = -0.1$, in Fig. 18(a).

Note that in order to maintain constant the Reynolds number while changing the polymer coefficient of viscosity, it was necessary to vary the fluid density.

5.4. Influence of inertia and three-dimensional flow characteristics

To understand the 3D characteristics of the flow within the smooth contraction, and the extension of the velocity overshoot phenomenon, we start by showing a three-dimensional view of the velocity profile, and its three orthogonal projections, as the fluid is about to enter the expansion, in Fig. 19. For this particular simulation the inlet velocity was lower ($U_b = 0.260$ m/s) than in the above simulations and in the experiments of Poole et al. [1,3] for a 0.1% PAA solution (ca. $U_b = 0.470$ m/s), leading to a lower Reynolds number, $Re = 2.8$. The velocity overshoot at the wall in the XZ-centreplane ($y/D = 0$) is clear, but the striking feature is the formation of strong velocity overshoots at the corners of the contraction. Simultaneously, close to those overshoots, in the proximity of the flat walls, small velocity depressions appear. In fact, these depressions were already apparent in some of the velocity profiles of Sections 5.1 and 5.2 that exhibited lower velocities next to the overshoots. The maxima at the corners of the contraction were unexpected and have not yet been report in experimental work.

These features called for a more extensive investigation on the effects of inertia. This was carried out with three sets of simulations the characteristics of which are listed in Table 2. Here, constitutive parameters were kept constant at values that facil-

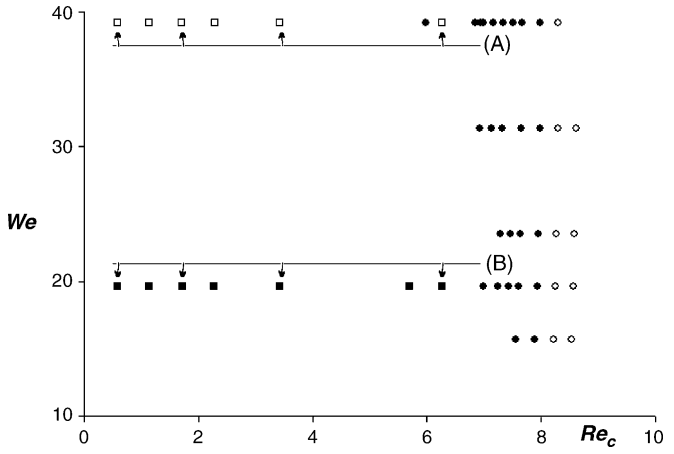

Fig. 20. Map of simulations with different fluid densities. Closed circles symbols represent the simulations with constant fluid density where velocity overshoots were found; open and closed squares symbols represent the simulations of set (a) and sets (b) and (c) in Table 2, respectively.

itate the appearance of velocity overshoots (such as $\varepsilon = 0.005$ and $\xi = 0.2$), but we also carried out simulations for conditions of low steady and transient extensional viscosity ($\varepsilon = 0.25$); the inertia was changed via the fluid density. Fig. 20 presents the corresponding map of simulations in the $We - Re_c$ space. The Reynolds number based on the characteristic shear rate at the backward facing step (Re_c), defined in Eq. (7), is used now to facilitate comparison with the experimental results. The map also includes the previous simulations at a constant Re, but variable Re_c, which are represented by circles, with the closed circles marking those cases for which velocity overshoots were observed.

Inertia was found to have a dramatic impact on the three-dimensional flow characteristics, as we can see in the three sets of 3D plots of Fig. 21. These 3D profiles are stills showing the status of the flow at the exit of the contraction, which were made from 3D movies showing the progression of the fluid along the contraction. The first set, in Fig. 21(a) pertains to a high Weissenberg number ($We = 39.2$) and intense strain-hardening of the extensional viscosity ($\varepsilon = 0.005$). Each three-dimensional velocity profile corresponds to a different Reynolds number, with the four simulations marked by arrows along the horizontal line A in Fig. 20. As the Reynolds number decreases the three-dimensional velocity profiles change dramatically. There are velocity overshoots at all Reynolds numbers near the flat side walls (on the XZ-centreplane), but they are small at $Re_c = 6.3$ and increase in magnitude and size as Re_c decreases. As Re_c decreases the velocity profiles become triangular and slim and the plateau at the centre of the duct disappears. Simultaneously, the peak velocities near the flat side walls became higher than those near the curved side walls and the maximum velocities increased (at $Re_c = 1.7$ and 0.58, u_{max}/U is around 1.5 and 1.8, respectively). The role of the Weissenberg number in enhancing these features is clear as it suffices to compare Fig. 21(a) (high We) and (b) (low We), especially at the lower range of Re_c. Note that Poole et al. [3] have also observed the appearance of a triangular shape velocity profile in their experimental measurements with 0.4% PAA, albeit at different Reynolds and Weissenberg numbers. What becomes clear is that this feature results from a combination of low Reynolds number and ε, with high Weissenberg number and high ξ.

Fig. 21(b) shows the same type of 3D velocity plots for the simulations marked with arrows along the horizontal line marked B in Fig. 20, corresponding to a lower Weissenberg number of 19.6. The flow features observed are qualitatively the same as at $We = 39.2$, but the overshoots are sharper, in agreement with the findings of Section 5.2 that We broadens the velocity over-

Table 2
Simulations with different fluid densities

Set	ε	λ	η_p	η_S	ξ	U	We	Re_c	Re	ρ
	0.005	0.6	0.5	0.05	0.2	0.39	39.23	0.58	0.43	100
	0.005	0.6	0.5	0.05	0.2	0.39	39.23	1.14	0.86	200
	0.005	0.6	0.5	0.05	0.2	0.39	39.23	1.71	1.28	300
(a)	0.005	0.6	0.5	0.05	0.2	0.39	39.23	2.28	1.71	400
	0.005	0.6	0.5	0.05	0.2	0.39	39.23	3.42	2.57	600
	0.005	0.6	0.5	0.05	0.2	0.39	39.23	5.70	4.28	1000
	0.005	0.6	0.5	0.05	0.2	0.39	39.23	6.28	4.70	1100
	0.005	0.25	0.5	0.05	0.2	0.47	19.61	0.58	0.48	94
	0.005	0.25	0.5	0.05	0.2	0.47	19.61	1.14	0.95	185
	0.005	0.25	0.5	0.05	0.2	0.47	19.61	1.71	1.42	277
(b)	0.005	0.25	0.5	0.05	0.2	0.47	19.61	2.28	1.90	369
	0.005	0.25	0.5	0.05	0.2	0.47	19.61	3.42	2.84	553
	0.005	0.25	0.5	0.05	0.2	0.47	19.61	5.70	4.74	922
	0.005	0.25	0.5	0.05	0.2	0.47	19.61	6.28	5.22	1015
	0.25	0.25	0.5	0.05	0.2	0.47	19.61	6.28	5.13	732
	0.25	0.25	0.5	0.05	0.2	0.47	19.61	5.70	4.60	665
	0.25	0.25	0.5	0.05	0.2	0.47	19.61	3.42	4.18	399
(c)	0.25	0.25	0.5	0.05	0.2	0.47	19.61	2.28	2.52	266
	0.25	0.25	0.5	0.05	0.2	0.47	19.61	1.71	1.67	200
	0.25	0.25	0.5	0.05	0.2	0.47	19.61	1.14	1.25	133
	0.25	0.25	0.5	0.05	0.2	0.47	19.61	0.58	0.83	68

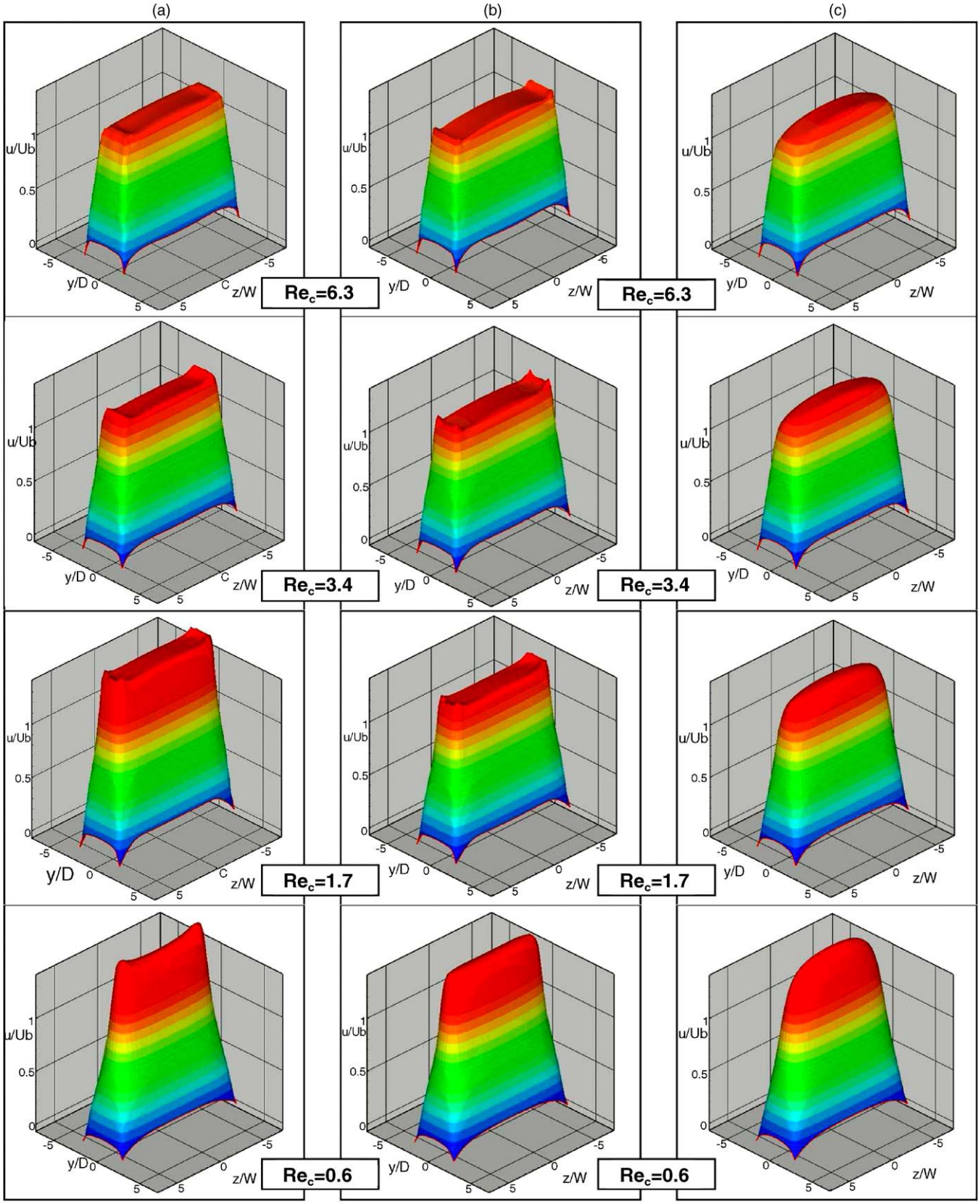

Fig. 21. 3D velocity profile in the smooth contraction at $x/h = -0.1$ for different Re_c number: $\xi = 0.2$: (a) $We = 39.2$, $\varepsilon = 0.005$; (b) $We = 19.6$, $\varepsilon = 0.005$; (c) $We = 19.6$, $\varepsilon = 0.25$.

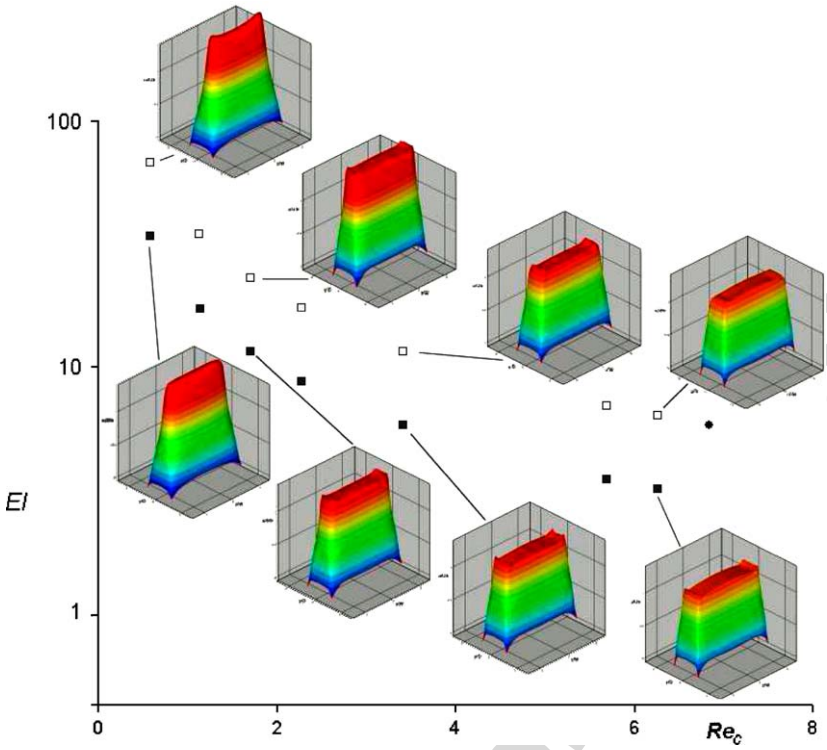

Fig. 22. Map of simulations in $El - Re_c$ space for $\xi = 0.2$, $\beta = 1/11$, $\varepsilon = 0.005$ and 3D velocity profiles. Closed circle: simulations for $Re = 5.14$ exhibiting velocity overshoots; open squares: simulations of set (a) in Table 2; closed squares: simulations of set (b) in Table 2.

shoots. For $Re = 3.4$ and $We = 19.6$ there are velocity overshoots at the duct corners which are slightly higher than elsewhere and in particular higher than at the mid-planes. Further decrease in Reynolds number eliminates the velocity overshoots leading to the triangular and slim velocity profiles, but we no longer see the slight decrease in velocity at the centre of the duct seen at $We = 39.2$.

To emphasize the role of strain-hardening of the extensional viscosity Fig. 21(c) plots results for the same Weissenberg number of 19.6 and $\xi = 0.2$, but with a higher value of $\varepsilon = 0.25$. In the map of Fig. 20, these four cases still correspond to the four arrows of line B. The reduction in strain-hardening of the extensional viscosity smoothes the velocity profile which no longer exhibit velocity overshoots at any of the Reynolds numbers. The velocity profiles are akin to those for pure viscous fluids, without the flat velocity region in the core. At low Reynolds numbers there are also no velocity overshoots but nevertheless there is a weak tendency for the velocity profile to become slim and triangular when viewed in the XY-centreplane. We may thus also conclude that flat velocity profiles result from a combination of inertia with high relaxation times not allowing stress relaxation to occur as the fluid undergoes a transient flow which is characterized by very low levels of vorticity almost everywhere except near the walls.

6. Conclusions

The flow inside a smooth contraction preceded by a square duct of viscoelastic fluids modeled by the PTT constitutive equation has many features which depend in a complex manner on memory effects, inertia, second normal-stress differences, shear-thinning and extensional viscosity. Undoubtedly, for this geometry the appearance of velocity overshoots with the PTT model requires non-negligible second normal-stress differences in shear and this has been demonstrated elsewhere [3]. Here, we were able to identify the other conditions required to observe velocity overshoots, although agreement with experiments was only qualitative, and we also show that the velocity overshoots are unrelated to the loss of monotonicity in the steady shear stress/shear rate of the PTT model since they were also found for values of $\beta > 1/9$. However, there can be a link between the velocity overshoots and the oscillating behaviour of transient shear properties and the clarification of this issue requires further research using finer meshes as well as other constitutive models.

An alternative map representating the simulations in this work is shown in Fig. 22, and includes some representative 3D velocity profiles at the exit of the contraction. The map plots the elasticity number $El = We/Re_c = \lambda\eta_c/\rho H^2$ as a function of the characteristic shear rate Reynolds number for $\xi = 0.2$, $\varepsilon = 0.005$ and $\beta = 1/11$. By using the elasticity number instead of the Weissenberg number, the kinematics is removed from this elasticity quantifier, which compares the relaxation and diffusion times of the fluid.

The range of Reynolds numbers in these simulations is quite narrow and yet significant changes were observed. At high values of the Reynolds numbers velocity overshoots are weak and tending to disappear if Re_c is increased further, and the velocity profiles are rather blunt at the centre of the duct. The simulations at higher El show broader peaks of velocity near the walls

than at lower values of *El*. At the intermediate range of values of *El* and Re_c in the plot, the velocity overshoots are at its strongest, appearing inside of the smooth contraction and there are also very intense overshoots at the corners of the duct, which remain after the end of the contraction. Finally, at low Reynolds numbers and high values of the elasticity number again no velocity overshoots are seen and the three-dimensional velocity profile becomes slim and triangular in shape when viewed on the *XY*-centreplane, developing also higher peaks near the flat side walls on account of the elasticity. So, it is at the intermediate range of *El* and Re_c that velocity overshoots are more intense.

Other important conclusions from our calculations were the following:

- There were convergence difficulties for simulations with low values of ξ, high *We* numbers and low values of ε, which did not allow us to completely understand the influence of ξ (the well-known high Weissenberg number problem). Nevertheless, it is clear that the formation of velocity overshoots on the *XZ*-centreplane in this smooth contraction requires high values of ξ in combination with high Weissenberg numbers, intermediate Reynolds numbers and shear-thinning. At the corners of the duct the overshoots are significantly more intense than at the mid-planes, for certain combinations of parameters.
- For high values of ξ strain-hardening of the extensional viscosity enhances the overshoots on the *XZ*-centreplane. As the Weissenberg number is increased the overshoots broaden and move towards the centre of the duct.
- With a low value of ε in combination with high values of *We* and ξ, the shape of the velocity profile in the *XY*-centreplane is qualitatively close to that seen experimentally by Poole et al. [1,3] with their 0.05% PAA solution.
- Shear-thinning further enhances the velocity overshoots in particular those in the *XY*-centreplane. Unfortunately, reducing parameter β leads to convergence difficulties.

We could not quantitatively simulate the experimental observations of Poole et al. [1,3], but qualitatively the observed features have been well captured with these single mode PTT model simulations. A more accurate description of the rheology of the fluids is clearly necessary for quantitative agreement, with particular care to represent well transient fluid characteristics, avoiding loss of monotonic behaviour in steady shear stress/shear rate and most probably requiring a multimode model.

Acknowledgments

The authors would like to acknowledge the financial support of FEDER and FCT through projects POCTI 37711/EME/2001 and POCI 56342/EQU/2004. We are grateful to Dr. Manuel Alves (University of Porto), Dr. Rob Poole and Prof. Marcel Escudier (both from the University of Liverpool) for helpful discussions as well as to one of the reviewers for his/her pertinent comments. The code used in these calculations was the finite volume code of Oliveira et al. [26], as improved by Alves et al. [27,28] and Afonso and Pinho [43].

References

[1] R.J. Poole, M.P. Escudier, A. Afonso, F.T. Pinho, Laminar viscoelastic flow over a backward-facing step, in: Proceedings of the XIV International Congress on Rheology, Paper NF-06, Seoul, South Korea, 2004.
[2] R.J. Poole, M.P. Escudier, P.J. Oliveira, Laminar flow of a viscoelastic shearthinning liquid through a plane sudden expansion preceded by a gradual contraction, Proc. R. Soc. London Series A 461 (2005) 3827–3845.
[3] R.J. Poole, M.P. Escudier, A. Afonso, F.T. Pinho, Laminar flow of a viscoelastic shear-thinning liquid over a backward-facing step preceded by a gradual contraction, Phys. Fluids, submitted for publication.
[4] A.L. Halmos, D.V. Boger, A. Cabelli, The behaviour of power-law fluid flowing through a sudden expansion. Part I. Numerical solution, AIChE J. 21 (1975) 540.
[5] A.L. Halmos, D.V. Boger, A. Cabelli, The behaviour of power-law fluid flowing through a sudden expansion. Part II. Experimental verification, AIChE J. 21 (1975) 550.
[6] F.T. Pinho, P.J. Oliveira, J.P. Miranda, Pressure losses in the laminar flow of shear-thinning power-law fluids across a sudden pipe expansion, Int. J. Heat Fluid Flow 24 (2003) 747–761.
[7] A.L. Halmos, D.V. Boger, Flow of viscoelastic polymer solutions through an abrupt 2-to-1 expansion, Trans. Soc. Rheol. 20 (1976) 253.
[8] P. Townsend, K. Walters, Expansion flows of non-Newtonian liquids, Chem. Eng. Sci. 49 (1994) 749.
[9] A. Baloch, P. Townsend, M.F. Webster, On vortex development in viscoelastic expansion and contraction flows, J. Non-Newtonian Fluid Mech. 65 (1996) 133.
[10] F. Durst, A. Melling, J.H. Whitelaw, Low Reynolds number flow over a plane sudden expansion, J. Fluid Mech. 64 (1974) 111.
[11] W. Cherdron, F. Durst, J.H. Whitelaw, Asymmetric flows and instabilities in symmetric ducts with sudden expansions, J. Fluid Mech. 84 (1978) 13.
[12] R.M. Fearn, T. Mullin, K.A. Cliffe, Nonlinear phenomena in a symmetric sudden expansion, J. Fluid Mech. 211 (1990) 595.
[13] D. Drikakis, Bifurcation phenomena in incompressible sudden expansion flows, Phys. Fluids 9 (1997) 76.
[14] E. Schreck, M. Schafer, Numerical study of bifurcation in three-dimensional sudden channel expansions, Comp. Fluids 29 (2000) 583.
[15] M.F. Letelier, D.A. Siginer, Secondary flows of viscoelastic liquids in straight tubes, Int. J. Solids Struct. 40 (2003) 5081–5095.
[16] J.P. Hartnett, M. Kostic, Heat transfer to Newtonian and non-Newtonian fluids in rectangular ducts, Adv. Heat Transfer 19 (1989) 247–355.
[17] S.X. Gao, J.P. Hartnett, Heat transfer behavior of Reiner–Rivlin fluids in rectangular ducts, Int. J. Heat Mass Transfer 39 (1996) 1317–1324.
[18] B. Debbaut, J. Dooley, Secondary motions in straight and tapered channels: experiments and three-dimensional finite element simulation with a multimode differential viscoelastic model, J. Rheol. 43 (6) (1999) 1525–1545.
[19] R.I. Tanner, Engineering Rheology, Section 4.1.13, Clarendon Press, Oxford, 1992.
[20] A.I. Leonov, A.N. Prokunin, Non-linear Phenomena in Flows of Viscoelastic Polymer Fluids, Sections 8.2 and 8.3, Chapman and Hall, New York, 1994.
[21] N. Phan-Thien, R.I. Tanner, A new constitutive equation derived from network theory, J. Non-Newt Fluid Mech. 2 (1977) 353.
[22] N. Phan-Thien, A non-linear network viscoelastic model, J. Rheol. 22 (1978) 259.
[23] G.H. McKinley, Discussion on new benchmark flows for viscoelastic 3D and transient computations, in: Communication at XIVth International Workshop of Numerical Methods for Non-Newtonian flows, Santa Fe, NM, USA, June 12–15, 2005.
[24] M.P. Escudier, S.E. Smith, Fully developed turbulent flow of Newtonian liquids through a square duct, Proc. R. Soc. London A 457 (2001) 911.
[25] M.A. Alves, P.J. Oliveira, F.T. Pinho, Benchmark solutions for the flow of Oldroyd-B and PTT fluids in planar contractions, J. Non-Newtonian Fluid Mech. 110 (2003) 45–75.

[26] P.J. Oliveira, F.T. Pinho, G.A. Pinto, Numerical simulation of non-linear elastic flows with a general collocated finite-volume method, J. Non-Newt Fluid Mech. 79 (1998) 1.
[27] M.A. Alves, F.T. Pinho, P.J. Oliveira, Effect of a high resolution differencing scheme on finite-volume predictions of viscoelastic flows, J. Non-Newt Fluid Mech. 93 (2000) 287.
[28] M.A. Alves, P.J. Oliveira, F.T. Pinho, A convergent and universally bounded interpolation scheme for the treatment of advection, Int. J. Numer. Meth. Fluids 41 (2003) 47.
[29] P.J. Oliveira, On the numerical implementation of nonlinear viscoelastic models in a finite-volume method, Numer. Heat Transfer B 40 (2001) 283.
[30] P.H. Gaskell, A.K.C. Lau, Curvature-compensated convective transport: SMART a new boundedness preserving transport algorithm, Int. J. Numer. Meth. Fluids 41 (1988) 617.
[31] C.G. Speziale, R.M.C. So, B.A. Younis, On the prediction of turbulent secondary flows, in: R.M.C. So, C.G. Speziale, B.E. Launder (Eds.), Near-Wall Turbulent Flows, Elsevier, 1993, pp. 105–114.
[32] J.A. Wheeler, E.H. Whissler, Steady flow of non-Newtonian fluids in a square duct, Trans. Soc. Rheol. 10 (1966) 353.
[33] P. Townsend, K. Walters, W.M. Waterhouse, Secondary flows in pipes of square cross-section and the measurement of second normal stress difference, J. Non-Newt Fluid Mech. 1 (1976) 107.
[34] B. Gervang, P.S. Larsen, Secondary flows in straight ducts of rectangular cross section, J. Non-Newt Fluid Mech. 39 (1991) 217.
[35] B. Debbaut, T. Avalosse, J. Dooley, K. Hughes, On the development of secondary motions in straight channels induced by the second normal stress difference: experiments and simulations, J. Non-Newt Fluid Mech. 69 (1997) 255.
[36] M. Siline, A.I. Leonov, On flows of viscoelastic liquids in long channels and dies, Int. J. Eng. Sci. 39 (2001) 415–437.
[37] A.G. Dodson, P. Townsend, K. Walters, Non-Newtonian flow in pipes of non-circular cross-section, Comput. Fluids 2 (1974) 317.
[38] M.M. Alves, F.T. Pinho, P.J. Oliveira, Study of pipe and channel flows of a single-mode Phan-Thien–Tanner fluid, J. Non-Newtonian Fluid Mech. 101 (2001) 55.
[39] G.C. Georgiou, D. Vlassopoulos, On the stability of the simple shear flow of a Johnson–Segalman fluid, J. Non-Newtonian Fluid Mech. 75 (1998) 77–97.
[40] M.A. Alves, Personal communication, 2006.
[41] D.D. Joseph, Fluid dynamics of viscoelastic liquids Applied Mathematic Sciences Series, vol. 84, Springer Verlag, Berlin, 1990.
[42] M.A. Hulsen, Numerical simulation of the divergent flow regime in a circular contraction flow of a viscoelastic fluid, Theor. Comput. Fluid Dyn. 5 (1993) 33.
[43] A. Afonso, F.T. Pinho, Numerical implementation of the full Phan-Thien–Tanner (PTT) constitutive equation, Internal Report of CEFT (in Portuguese), University of Porto (FEUP), 2004.